

Numerical simulation of static and sliding drop with contact angle hysteresis

Jean-Baptiste Dupont, Dominique Legendre *

Université de Toulouse, INPT, UPS, Institut de Mécanique des Fluides de Toulouse (IMFT), Allée Camille Soula, F-31400 Toulouse, France
CNRS, IMFT, F-31400 Toulouse, France

ARTICLE INFO

Article history:

Received 5 May 2008

Received in revised form 23 July 2009

Accepted 29 July 2009

Available online 4 August 2009

Keywords:

Contact line

Fluid droplet

Partial wetting

Hysteresis

Dynamic angle

ABSTRACT

A numerical “macroscopic-scale” method for static (including hysteresis) and moving contact lines for partially wetting liquids is presented. The numerical method is based on the implementation of a “sub-grid” description of the contact line that consists in imposing the apparent angle for static and moving contact lines. The numerical simulations are validated against several well controlled bi-dimensional situations: the equilibrium shape of a drop released on a hydrophobic or hydrophilic wall, the axisymmetric spreading of a drop for a partially wetting liquid, the migration of a drop placed on a inclined wall and submitted to a Couette or Poiseuille flow.

© 2009 Elsevier Inc. All rights reserved.

1. Introduction

Despite its apparent simplicity, the behavior of a drop spreading on a wall is a very difficult problem. Indeed the wetting of a solid by a liquid concerns scales from the capillary length to the Van der Waals forces and remains only partially understood [4,17,24]. The description of the contact line (where the fluid–fluid interface intersects the solid surface) is complicated by the fact that the Navier–Stokes equations with standard no-slip conditions produce an infinite viscous dissipation [28]. Consequently a microscopic description has to be introduced to cut of this singularity. From the numerical point of view, this particular complexity of the physics of the contact line makes the simulations very delicate. For instance, the numerical description of the deformation and the motion of a drop on an inclined wall or submitted to a shear flow requires a numerical model able to simulate the static deformation of the drop, the transition from the static to the motion and then the motion of the receding and advancing contact lines. Only recently methods have been developed to account for the numerical implementation of the hysteresis and the dynamics of the contact angle, the angle that the fluid–fluid interface makes with the solid surface at the contact line. Few numerical studies presented in the literature are able to describe the complete behavior of the contact line (see [55] for a recent review on the subject). The numerical studies differ: (i) by the numerical strategy used to describe the interface displacement and deformation: Boundary Integral Method [14,27,52], Adaptive grid methods [21,53], Level Set Method [38,55], Volume of Fluid Method [1,47] or Front-Tracking Method [31]; (ii) by the way that the moving contact angle is imposed: constant angle with no-slip conditions [1,31,47], static angle with a “slip length” [2,38,55], dynamic model for the apparent angle [27], Diffuse Interface Method [15,29]. Moving contact lines have also been modeled with contact angle hysteresis in two-dimensional situations [38,55] and three-dimensional situations [16]. Most of these approaches do not describe the microscopic (Van der Waals) interactions between the fluids and the solid wall but solve the

* Corresponding author.

E-mail address: legendre@imft.fr (D. Legendre).

flow on a macroscopic-scale to access to large scale of the interface. The limitation of such numerical approach is that it is not possible to perform direct numerical simulations of the flow up to the molecular scale responsible for the wetting as Molecular Dynamics simulations can do [4]. For macroscopic-scale simulations, adapted models have to be selected and implemented to describe the contact angle at a sub-grid scale. This is the objective of the numerical approach presented in this paper. We present a numerical method to describe static (including hysteresis) and moving contact lines for partially wetting liquids. The numerical code JADIM used for this study and the numerical modeling introduced to describe the physics of the contact line are presented in Sections 2 and 3, respectively. Section 4 presents numerical tests performed to characterize the spurious currents for isolated and wetting drops. In Section 5, the numerical modeling of the contact line is validated by considering the equilibrium shape of a drop deposited on hydrophobic or hydrophilic walls. The implementation of the dynamic angle is tested in Section 6 by computing the axisymmetric spreading of a drop for a partially wetting liquid. In Section 7 we consider the two-dimensional problem of a drop initially placed on a horizontal wall which is slowly inclined until the motion of the drop. Finally, we consider in Section 8 the deformation and the migration of two-dimensional drops submitted to a shear flow.

2. Numerical method

The numerical code used for this study is the JADIM code developed to perform local analyses of dispersed two-phase flows [34,35,41,43]. The objective of this work is to introduce the modeling of the contact line in the Volume of Fluid (VoF) modulus of JADIM [3,7,8]. The implemented VoF method consists in an Eulerian description of each phase on a fixed grid, the interface between the two-phases being calculated using the transport equation of the local volume fraction of one phase. The two fluids are assumed to be Newtonian and incompressible with no phase change. Under isothermal condition and in the absence of any surfactant the surface tension is constant and uniform at the interface between the two fluids. In such conditions, the velocity field \mathbf{U} and the pressure P satisfy the classical one-fluid formulation of the Navier–Stokes equations:

$$\nabla \cdot \mathbf{U} = 0 \quad (1)$$

$$\rho \left(\frac{\partial \mathbf{U}}{\partial t} + (\mathbf{U} \cdot \nabla) \mathbf{U} \right) = -\nabla P + \nabla \cdot \boldsymbol{\Sigma} + \rho \mathbf{g} + \mathbf{F}_s \quad (2)$$

where ρ and μ are the density and dynamical viscosity. $\boldsymbol{\Sigma}$ is the viscous stress tensor, \mathbf{g} is the gravity and \mathbf{F}_s is the capillary contribution:

$$\mathbf{F}_s = -\sigma (\nabla \cdot \mathbf{n}) \mathbf{n} \delta_I \quad (3)$$

where σ is the surface tension, \mathbf{n} denotes the unit normal of the interface going out from phase 1 and δ_I is the Dirac distribution associated to the interface. The location of each phase is given by a scalar C (called volume fraction or color function) which obeys the transport equation:

$$\frac{\partial C}{\partial t} + \mathbf{U} \cdot \nabla C = 0 \quad (4)$$

This volume fraction is $C = 1$ (resp. $C = 0$) in cells filled with fluid 1 (resp. 2) and $0 < C < 1$ in cells cut by the interface. The local density and dynamic viscosity are deduced from the value of C by a linear interpolation

$$\rho = C\rho_1 + (1 - C)\rho_2 \quad \mu = C\mu_1 + (1 - C)\mu_2 \quad (5)$$

The specific aspect of our approach when compared to the classical VoF or Level Set Methods [49–51] concerns the technique used to control the thickness of the interface. In our approach no interface reconstruction or redistance techniques are introduced. The interface location and thickness are both controlled by an accurate transport algorithm based on Flux-Corrected Transport (FCT) schemes [58]. This method leads to an interface thickness of about three grid cells by the implementation of a specific procedure for the velocity used to transport C in flow region of strong strain and shear [8].

The numerical description of the surface tension is one of the crucial points to study systems where capillary effects control the interface shape. This interfacial force is solved using the classical Continuum Surface Force (CSF) model [9] and is distributed over grid points neighboring the interface. It means to transform a surface force \mathbf{F}_s into a force \mathbf{F}_v by spreading its effect in a region of thickness of few cells:

$$\mathbf{F}_v = -\sigma \nabla \cdot \left(\frac{\nabla C}{\|\nabla C\|} \right) \nabla C \quad (6)$$

The expression of the capillary term is composed of two terms representing, respectively the curvature $\nabla \cdot (\nabla C / \|\nabla C\|)$ and the location/orientation ∇C of the capillary forcing. A classical problem of this formulation is the generation of spurious currents [32,46] due to an inaccurate calculation of the curvature of the interface. In order to decrease spurious current intensity, a classic solution introduced by Brackbill et al. [9] consists of calculating the surface curvature from a smoothed density gradient whilst the discretisation of the delta function uses an unsmoothed density. Popinet and Zaleski [46] propose a “pressure-gradient” correction, Lafaurie et al. [32] implemented a conserving form of the surface tension term and Jamet

et al. [30] developed an energy conserving discretisation in a Second-Gradient method. Renardy and Renardy [48] have implemented the Parabolic Reconstruction Of Surface Tension (PROST) method in the SURFER code that reduced the magnitude of the spurious currents. More recently, François et al. [22] have developed the Sharp Surface tension Force (SSF) method that also significantly reduces spurious currents compared to CSF methods. In our approach the capillary term is calculated by imposing successive filtering to the volume fraction (here in two dimensions):

$$\hat{C}_{ij}^{n_f} = \frac{3}{4} \hat{C}_{ij}^{n_f-1} + \frac{1}{16} (\hat{C}_{i+1,j}^{n_f-1} + \hat{C}_{i-1,j}^{n_f-1} + \hat{C}_{i,j+1}^{n_f-1} + \hat{C}_{i,j-1}^{n_f-1}) \quad (7)$$

with $n_f = 1, \dots, N$ and $\hat{C}_{ij}^0 = C_{ij}$. The capillary force is then evaluated using the smoothed distribution $\hat{C} = \hat{C}^N$. The number of iterations N required to significantly reduce spurious currents and to obtain accurate results has been first tested in unbounded fluid at rest [6]. Additional tests have been performed in this study for static isolated drops and drops wetting a plane surface. These are presented in Section 4. The filtering of each contribution to the capillary term has been tested separately, N_K and N_L being the number of iterations in the filtering procedure applied to C to calculate the curvature and the location/orientation contributions, respectively. The equations are discretized on a staggered grid using a finite volume method, all spatial derivatives being approximated using second-order centered schemes. The volume fraction C and the pressure P are volume-centered and the velocity components are face-centered. Time advancement is achieved through a third-order Runge–Kutta method for advective and source terms and a Crank–Nicolson method for viscous stresses. Incompressibility is satisfied at the end of each time step through a projection method. The overall algorithm is second-order accurate in both time and space. Basically each time step is composed of four steps. Hence starting with \mathbf{U}^n and C^n they are:

Step 1. Update for C

The advection Eq. (4) is solved by using a modified version of the transport scheme proposed by Zalesak [58]. The procedure to transport the interface is described in detail in [8]. Briefly, the fronts are prevented from spreading in time by a specific strategy in which the velocity at nodes crossed by the interface is modified to keep the thickness of the interface constant. The velocity used to transport C is made almost constant across the interface by using the velocity interpolated at $C = 0.5$. The intermediate value of the volume fraction is used to obtain:

$$\rho^{n+1/2} = C^{n+1/2} \rho_1 + (1 - C^{n+1/2}) \rho_2, \quad \mu^{n+1/2} = C^{n+1/2} \mu_1 + (1 - C^{n+1/2}) \mu_2 \quad (8)$$

Step 2. Semi-implicit viscous solve for \mathbf{U}^*

In this step, an intermediate velocity field \mathbf{U}^* is computed from changes to the known field \mathbf{U}^n which result from convective, viscous and body forces. This is achieved using a three-step Runge–Kutta (RK) time-stepping procedure where the nonlinear advective terms A are computed explicitly while the diffusive terms L are treated using the semi-implicit Crank–Nicolson (CN) algorithm (see [10,34]). Within each of the three intermediate steps ($k = 1, 2, 3$) of the time step $[n\Delta t, (n+1)\Delta t]$ the solution is advanced as follows:

$$\frac{\mathbf{U}^k - \mathbf{U}^{k-1}}{\Delta t} = \gamma_k A(\mathbf{U}^{k-1}) + \zeta_k A(\mathbf{U}^{k-2}) + (\alpha_k + \beta_k) \left[\mathbf{g} - \frac{1}{\rho^{n+1/2}} \nabla P^{n-1/2} \right] + (\alpha_k + \beta_k) L(\mathbf{U}^{k-1}) + \beta_k L(\mathbf{U}^k - \mathbf{U}^{k-1}) \quad (9)$$

where $\mathbf{U}^0 = \mathbf{U}^n$ and $\mathbf{U}^3 = \mathbf{U}^*$. The Runge–Kutta coefficients $\alpha_k, \beta_k, \gamma_k$ and ζ_k are those currently used in the RK/CN algorithm (see [10]).

Step 3. Capillary contribution for \mathbf{U}^{**}

A second intermediate velocity field \mathbf{U}^{**} is introduced to determine the capillary contribution:

$$\frac{\mathbf{U}^{**} - \mathbf{U}^*}{\Delta t} = \frac{1}{\rho^{n+1/2}} \mathbf{F}_v^{n+1/2} \quad (10)$$

The capillary term $\mathbf{F}_v^{n+1/2}$ given by (6) is evaluated by approximating the smoothed distribution $\hat{C} = \hat{C}^N$ at time $(n+1/2)\Delta t$. The value of the contact angle $\theta^{n+1/2}$ is determined following the procedure described in the next section. Briefly, the value of the contact angle θ^* that locally cancels \mathbf{U}^{**} is calculated using an iterative procedure. If $\theta_R \leq \theta^* \leq \theta_A$, θ is imposed to be θ^* , otherwise θ is calculated using the dynamic model chosen for this study.

Step 4. Projection step for \mathbf{U}^{n+1}

The final velocity field \mathbf{U}^{n+1} is made divergence-free by solving

$$\frac{\mathbf{U}^{n+1} - \mathbf{U}^{**}}{\Delta t} = -\frac{1}{\rho^{n+1/2}} \nabla \Phi^{n+1/2} \quad (11)$$

where the pressure correction $\Phi^{n+1/2}$ is solution of the pseudo-Poisson equation:

$$\nabla \cdot \left(\frac{1}{\rho^{n+1/2}} \nabla \Phi^{n+1/2} \right) = -\frac{\nabla \cdot \mathbf{U}^{**}}{\Delta t} \quad (12)$$

The final pressure is deduced from the auxiliary potential $\Phi^{n+1/2}$ through the relation:

$$P^{n+1/2} = P^{n-1/2} + \Phi^{n+1/2} \quad (13)$$

The linear system (12) is solved by a Jacobi preconditioned conjugate gradient technique (The JCG of the ITPACK Library) for three-dimensional cases while a direct Cholesky method is used in two-dimensional situations [41].

3. Numerical modeling of the contact angle

The main challenge for numerical simulations of drops spreading on surfaces concerns the accurate description of the surface tension effects controlled by the hysteresis and the motion of contact lines on walls. The numerical model for the contact angle developed in this study is presented in the following. We would like to stress here that the interface is not reconstructed in our approach so that it is not possible to impose directly the slope of the interface (or its normal) in the cell touching the wall. Our objective is to develop an accurate simulation of the physics of the wetting in order to impose the correct apparent (macroscopic) angle θ at a wall for any instantaneous situation (Fig. 1). This could be a static situation with an angle in the interval defined by the advancing angle θ_A and the receding angle θ_R ($\theta_R \leq \theta \leq \theta_A$) or a dynamic situation for a moving line with a instantaneous dynamic angle $\theta_d(t)$ determined with an adapted model.

3.1. Numerical procedure to impose a given angle

As shown by expression (6), the capillary contribution to the momentum equation requires the knowledge of ∇C . If we denote the apparent (macroscopic) angle θ between the interface and the wall, the value of ∇C at the wall is linked to the normal \mathbf{n} of the interface by the relation:

$$\frac{\nabla C}{\|\nabla C\|} = \mathbf{n} = \sin\theta \mathbf{n}_{\parallel} + \cos\theta \mathbf{n}_{\perp} \quad (14)$$

where \mathbf{n}_{\parallel} and \mathbf{n}_{\perp} are unit vectors parallel and normal to the wall, respectively (Fig. 2).

In practice, the value of ∇C at the wall is obtained using a “ghost” value C_w of the void fraction at the wall. If we consider a wall of normal \mathbf{e}_z , the ghost value $C_{i,w}$ is deduced from the calculated value $C_{i,k}$ and $C_{i,k+1}$ at points k and $k+1$, respectively:

$$C_{i,w} = \frac{\delta_2^2}{\delta_2^2 - \delta_1^2} C_{i,k} - \frac{\delta_1^2}{\delta_2^2 - \delta_1^2} C_{i,k+1} - \frac{\delta_2 \delta_1}{\delta_2 + \delta_1} \left(\frac{\partial C}{\partial z} \right)_{i,w} + O(\delta^3) \quad (15)$$

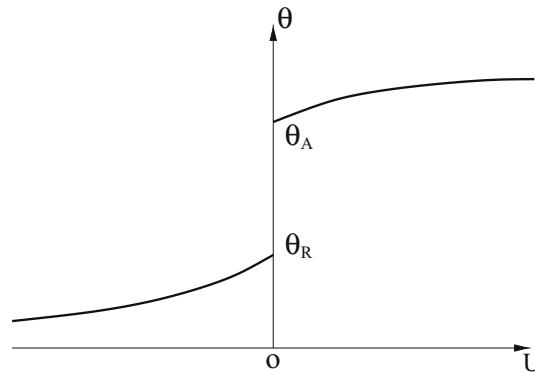


Fig. 1. Evolution of the apparent angle θ of the interface with the contact-line velocity (after [17]).

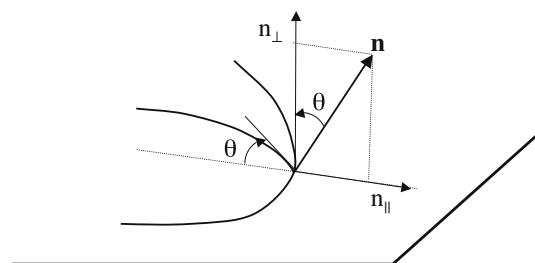


Fig. 2. Definition of the normal of the interface at the contact line.

where δ_2 and δ_1 are the distances from the wall of nodes C_k and C_{k+1} , respectively. For a regular grid spacing Δ normal to the wall, $\delta_2 = 3\Delta/2$ and $\delta_1 = \Delta/2$, and the terms involving δ_2 and δ_1 in (15) are $9/8, 1/8$ and $3\Delta/8$, respectively. The derivative normal to the wall $(\partial C/\partial z)_{i,w}$ has to be determined so that the calculation of ∇C at the wall satisfies the relation (14) that guaranties the angle θ between the interface and the wall.

For example, if we consider the 2D situation ($\mathbf{e}_x, \mathbf{e}_z$) where the normal of the wall is \mathbf{e}_z , one has $\mathbf{n}_{\parallel} = \mathbf{e}_x$ and $\mathbf{n}_{\perp} = \mathbf{e}_z$. We deduce from (14) the relation at the wall that satisfies $(\partial C/\partial z)_{i,w}$:

$$\left(\frac{\partial C}{\partial z}\right)_{i,w} \sin\theta = -\left|\frac{\partial C}{\partial x}\right|_{i,w} \cos\theta \quad (16)$$

The derivative $(\partial C/\partial x)_{i,w}$ is determined following a discretisation consistent with that used to determine the components of ∇C at the wall for the calculation of the capillary term (6). This is done by extrapolating the values $(\partial C/\partial x)_{i,k}$ and $(\partial C/\partial x)_{i,k+1}$ obtained using, respectively $C_{i,k}, C_{i-1,k}, C_{i+1,k}$ and $C_{i,k+1}, C_{i-1,k+1}, C_{i+1,k+1}$ to respect the second-order accuracy of the spatial discretization. Finally, the ghost value $C_{i,w}$ is calculated by:

$$C_{i,w} = \frac{\delta_2^2}{\delta_2^2 - \delta_1^2} C_{i,k} - \frac{\delta_1^2}{\delta_2^2 - \delta_1^2} C_{i,k+1} + \frac{\delta_2 \delta_1}{\delta_2 + \delta_1} \frac{\cos\theta}{\sin\theta} \left|\frac{\partial C}{\partial x}\right|_{i,w} \quad (17)$$

Note that this explicit procedure can be directly extended to 3D configurations. For example, considering the 3D situation of an interface wetting a wall of normal \mathbf{e}_z , relation (14) gives:

$$\left(\frac{\partial C}{\partial z}\right)_w \sin\theta = \left(\frac{\partial C}{\partial x}\right)_w \cos\theta n_{\parallel x} + \left(\frac{\partial C}{\partial y}\right)_w \sin\theta n_{\parallel y} \quad (18)$$

where $n_{\parallel x}$ and $n_{\parallel y}$ are the Cartesian component of \mathbf{n}_{\parallel} given by:

$$n_{\parallel x} = \frac{-\frac{\partial C}{\partial x}}{\sqrt{\left(\frac{\partial C}{\partial x}\right)_w^2 + \left(\frac{\partial C}{\partial y}\right)_w^2}}, \quad n_{\parallel y} = \frac{-\frac{\partial C}{\partial y}}{\sqrt{\left(\frac{\partial C}{\partial x}\right)_w^2 + \left(\frac{\partial C}{\partial y}\right)_w^2}} \quad (19)$$

and the ghost value at the wall is obtained by:

$$C_{i,w} = \frac{\delta_2^2}{\delta_2^2 - \delta_1^2} C_{i,j,k} - \frac{\delta_1^2}{\delta_2^2 - \delta_1^2} C_{i,j,k+1} + \frac{\delta_2 \delta_1}{\delta_2 + \delta_1} \frac{\cos\theta}{\sin\theta} \sqrt{\left(\frac{\partial C}{\partial x}\right)_{i,w}^2 + \left(\frac{\partial C}{\partial y}\right)_{i,w}^2} \quad (20)$$

The main interest of this approach is its generality that allows it to be used for any non-reconstruction interface algorithm whatever the numerical diffusion of the interface. The ghost value C_w given by (15) is imposed in all the cells containing the interface ($0 < C < 1$). This is important to stress that C_w is only used for the calculation of the capillarity term (6) in the momentum Eq. (2). Note also that the condition $(\partial C/\partial z)_w = 0$ is equivalent to consider an interface normal to the wall $\theta = 90^\circ$.

A possible improvement of this explicit method consists in calculating $(\partial C/\partial z)_{i,w}$ using the ghost values $C_{i-1,w}, C_{i,w}$ and $C_{i+1,w}$. Combined with relation (15) one then obtains a linear system for C_w .

3.2. Physical model for moving contact lines

Different models are available in the literature to describe contact line dynamics [5,20,24–26,45,54]. They differ by the approach used to solve the paradox of the contact line revealed by the continuum approach [4]. For this study, we have selected the hydrodynamic model developed by Voinov [57] and Cox [13] and Dussan's group [18,45]. According to [45], the contact angle of a moving interface is constant at a characteristic intermediate length scale $r \approx 10 \mu\text{m}$ between the microscopic length scale $l_m \approx 1 \text{ nm}$ where the microscopic angle is controlled by the intermolecular forces and the macroscopic length scale corresponding to the capillarity length $L_c = (\sigma/\Delta\rho g)^{1/2} \approx 1 \text{ mm}$ (Fig. 3). Several experimental studies have confirmed the size of these characteristic length scales [18,42,45,53]. The so-called dynamic angle θ_d depends on the slip

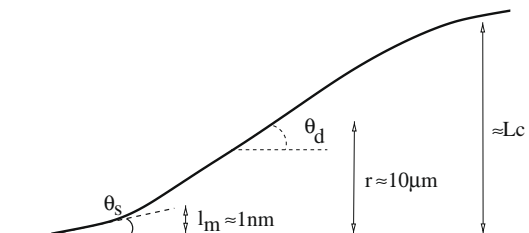


Fig. 3. Characteristic length scales for the apparent dynamic angle θ_d . l_m is the microscopic length, L_c is the macroscopic or capillarity length (after [4]).

velocity normal to the contact line at the wall $U_{cl} = \mathbf{U} \cdot \mathbf{n}_{\parallel}$ and can be expressed as a function of the slip capillary number Ca_{cl} [45]:

$$\theta_d(r) = g^{-1} \left[g(\theta(l_m)) + Ca_{cl} \ln \frac{r}{l_m} \right] \quad \text{with} \quad g(\theta') = \int_0^{\theta'} \frac{\theta - \sin \theta \cos \theta}{2 \sin \theta} d\theta \quad (21)$$

Note that this expression can be well approximated by the relation $\theta_d^3 = \theta(l_m)^3 + 9Ca_{cl} \ln(r/l_m)$ [13]. This model is valid under the conditions

$$Re_{cl} = \frac{\rho_L |U_{cl}| r}{\mu_L} \ll 1 \quad \text{and} \quad Ca_{cl} = \frac{\mu_L |U_{cl}|}{\sigma} \ll 1 \quad (22)$$

[11,33] have shown experimentally that the limit of validity is less restrictive: $Ca_{cl} \leq 0.1$. This aspect is discussed in Section 6 presenting numerical simulations of partial wetting dynamics. In our approach, we have decided to impose the apparent dynamic angle θ_d for the interface at the wall. The dynamic angle θ_d is obtained using the Dussan's model given by (21). The functions g and g^{-1} are calculated using the simplified expressions $g \approx x^3/9 - 0.00183985x^{4.5} + 1.845823 \times 10^{-6} x^{12.258487}$ and $g^{-1} \approx (9x)^{1/3} + 0.0727387x - 0.0515388x^2 + 0.00341336x^3$ proposed by Mathieu [40]. To be consistent with the selected physical model, the apparent angle has to be imposed at the intermediate distance $r \sim 10 \mu\text{m}$ so that the grid size Δ at the wall has to satisfy:

$$\Delta \sim r \sim 10 \mu\text{m} \quad (23)$$

In addition, a slip condition is used. The fluid is allowed to slide across the solid surface, following the Navier slip law [44]

$$U_w = \lambda \left(\frac{\partial U}{\partial z} \right)_w \quad (24)$$

where wall slip is quantified by a slip length λ which is the fictitious distance below the slipping surface where the velocity extrapolates to zero. Numerically, the slip boundary condition (24) is implemented in the following manner [37]. Evaluating the Taylor expansion of the velocity gradient at the wall $(\partial U / \partial z)_w$ at the centre of the first two rows of cells surrounding the wall (i.e. at distances $z = \delta_1$ and $z = \delta_2$ ($\delta_1 < \delta_2$) from the surface), allows us to obtain a second-order accurate expression of $(\partial U / \partial z)_w$:

$$\left(\frac{\partial U}{\partial z} \right)_w = -\frac{\delta_1 + \delta_2}{\delta_1 \delta_2} U_w + \frac{\delta_2}{\delta_1 (\delta_2 - \delta_1)} U_1 - \frac{\delta_1}{\delta_2 (\delta_2 - \delta_1)} U_2 \quad (25)$$

where $U_1 = U(z = \delta_1)$ and $U_2 = U(z = \delta_2)$. Then, combining (25) with the second of (24), the surface velocity U_w is obtained as

$$U_w = \left(\frac{\delta_2}{\delta_1 (\delta_2 - \delta_1)} U_1 - \frac{\delta_1}{\delta_2 (\delta_2 - \delta_1)} U_2 \right) / \left(\frac{1}{\lambda} + \frac{\delta_1 + \delta_2}{\delta_1 \delta_2} \right) \quad (26)$$

Using (26), the velocity gradient at the wall $(\partial U / \partial z)_w$ involved in the local momentum balance (viscous shear stress contribution) is obtained through the above approximation (25). The use of the Navier slip condition for solving moving contact line is discussed in Section 6.

3.3. Numerical implementation of hysteresis and dynamic angle

Due to hysteresis, the angle of the contact line depends on the direction of displacement of the interface. Indeed, when a drop is located on a wall which is progressively inclined, the drop deforms and only moves beyond a critical inclination of the wall α (see Section 7). The front angle increases progressively until it reaches the advancing angle θ_A corresponding to the motion of the contact line at this point. At the rear of the drop, the surface also deforms so that the angle decreases until it reaches the receding angle θ_R . The range of angles between θ_R and θ_A corresponds to the hysteresis of the contact line which is defined by:

$$U_{cl} < 0 \quad \text{if} \quad \theta_d < \theta_R \quad (27)$$

$$U_{cl} = 0 \quad \text{if} \quad \theta_R \leq \theta_d \leq \theta_A \quad (28)$$

$$U_{cl} > 0 \quad \text{if} \quad \theta_A < \theta_d \quad (29)$$

In the code we do not impose the value of the contact line velocity U_{cl} . The value of U_{cl} as well as the direction of displacement of the interface come from the momentum balance. First, we determine the value of the contact angle. The procedure consists in calculating the angle θ^* that cancels the local momentum balance (relation (10), intermediate step 3) in the cells in contact with the wall and cut by the interface. For this purpose, the value of the contact angle θ^* is determined by an iterative procedure and after convergence the following situations are tested:

- (i) if $\theta_R \leq \theta^* \leq \theta_A$, the contact angle with the wall is imposed as $\theta^{n+1} = \theta^*$. The ghost value of the void fraction C_w at the wall is calculated using (15) with $\theta = \theta^*$ so that the momentum (Eq. (10)) locally cancel. If the interface is immobile at the beginning of the time step, it remains immobile for the next time step; if the interface was previously in motion, the interface is stopped.
- (ii) if $\theta^* < \theta_R$ (resp. $\theta^* > \theta_A$), the limit of equilibrium is reached. The value of the contact angle θ^{n+1} is then calculated using the dynamic model (21) and it is used to calculate \mathbf{U}^{**} with Eq. (10). As indicated above, the velocity used to transport C is constant across the interface and corresponds to the velocity interpolated at $C = 0.5$. This velocity is used to determine U_{cl}^n for the calculation of the dynamic angle. Note that, if the interface was previously at rest ($U_{cl}^n = 0$), Eq. (21) gives $\theta^{n+1} = \theta_R$ (resp. $\theta^{n+1} = \theta_A$) for a receding (resp. advancing) contact line.

Consequently for hysteresis situations, the contact angle and the velocity of the contact line U_{cl} are not imposed but are calculated from the local momentum balance. This procedure allows the surface to naturally start to move when the local momentum cannot cancel with an angle θ^* ranging from θ_R to θ_A or to stop when the local momentum cancels with θ^* in the interval $\theta_R - \theta_A$. To prevent interface instability and diffusion at the contact line, the value of θ is first determined for $C = 0.5$ and is then imposed in all the cells $0 < C < 1$ along the direction \mathbf{n}_\parallel determined using (19) in agreement with the procedure developed to transport C .

3.4. Numerical validations

The validation of the Navier–Stokes solver of JADIM has been described in many previous studies dealing with particle or bubble hydrodynamics using boundary fitted domains (see for example [34–36,41,43]). The ability of the Volume of Fluid (VoF) modulus of JADIM to simulate the deformation and motion of fluid–fluid interfaces has been presented in [3,7,8] for unbounded dispersed two-phases flows. We present in the following of the paper additional tests in order to validate the new procedure developed to simulate problems controlled by contact line. Simulations have been performed in simple 2D (plane or axisymmetric) configurations for which analytical asymptotic solutions, numerical results or experimental data are available. The next section is devoted to the characterization of spurious currents.

4. Spurious currents characterization

The surface tension contribution in the momentum equation is calculated using the CSF method of [9]. The CSF method has the property to generate artificial flows called “spurious currents”. The aim of this section is to characterize these unphysical flows for isolated and wetting drops. For this purpose we consider situations of drops at equilibrium corresponding to exact solutions characterized by a zero velocity field at any time. The interface has also a constant curvature so that the pressure is uniform inside the drop. The discussion is presented by considering the ℓ_∞ and ℓ_1 norms of the spurious velocities defined by Renardy and Renardy [48] and Francois et al. [22]:

$$\ell_\infty = \max_{i,j,k} (\|\mathbf{U}_{i,j,k}\|) \quad \ell_1 = \frac{1}{N_x N_y N_z} \sum_{i,j,k} \|\mathbf{U}_{i,j,k}\|$$

For 2D cases, $N_z = 1$ and the summation over k is obviously frozen. Following [22] we also give a quantitative comparison between our numerical results and the exact solution. For this purpose, we compare the pressure jump across the interface with the theoretical one. From the numerical pressure field, the pressure jump is evaluated using three different ways:

- (1) $\Delta P_0 = P_0^{in} - P_\infty^{out}$ where P_0^{in} and P_∞^{out} are the values of the pressure at the drop center and the minimum pressure on the boundary of the computational domain, respectively.
- (2) $\Delta P_{total} = P_{total}^{in} - P_{total}^{out}$ where P_{total}^{in} and P_{total}^{out} are the averaged values of the pressure inside ($1 \geq C \geq 0.5$) and outside ($0.5 \geq C \geq 0$) the drop, respectively.
- (3) $\Delta P_{partial} = P_{partial}^{in} - P_{partial}^{out}$ where $P_{partial}^{in}$ and $P_{partial}^{out}$ are the averaged values of the pressure inside and outside, calculated for $1 \geq C \geq 0.95$ and $0.05 \geq C \geq 0$, respectively. Compared to ΔP_{total} , $\Delta P_{partial}$ does not include the evolution of the pressure across the diffused interface.

The corresponding relative errors are evaluated as: $E_0 = |\Delta P_0 - \Delta P_{exact}| / \Delta P_{exact}$, $E_{total} = |\Delta P_{total} - \Delta P_{exact}| / \Delta P_{exact}$ and $E_{partial} = |\Delta P_{partial} - \Delta P_{exact}| / \Delta P_{exact}$, respectively. The exact jump in pressure is $\Delta P_{exact} = 2\sigma/R$ in 3D and $\Delta P_{exact} = \sigma/R$ in 2D where R is the radius of the interface.

4.1. Spherical drop at equilibrium

The first configuration is a 3D test case presented by Renardy and Renardy [48]. These authors compare 3 methods called Continuum Surface Force (CSF), Continuous Surface Stress (CSS) and Parabolic Reconstruction Of Surface Tension (PROST) implemented in the SURFER code [32]. The computational domain is $L_x \times L_y \times L_z = 1 \times 1 \times 1$, the grid spacing is uniform $\Delta x = \Delta y = \Delta z = L_x/96$ and the time step is $\Delta t = 10^{-5}$. The number of time steps is $N_t = 200$. The boundary conditions are

Table 1

Norms of velocity and error in the pressure jumps at 200th time step ($\Delta t = 10^{-5}$). $\rho_L = \rho_G = 4$, $\mu_L = \mu_G = 1$ and $\sigma = 0.357$.

Method	ℓ_∞	ℓ_1	E_{total} (%)	$E_{partial}$ (%)	E_0 (%)
CSF@SURFER	0.0017998	0.00008403	–	–	–
CSS@SURFER	0.0037704	0.00014183	–	–	–
PROST@SURFER	0.0000224	0.00000087	–	–	–
CSF@JADIM					
$N_K, N_L = 0, 0$	0.0075949	0.00004189	5.1	0.8	0.6
$N_K, N_L = 6, 0$	0.0048164	0.00002726	5.9	0.5	0.4
$N_K, N_L = 12, 0$	0.0038810	0.00002120	6.0	0.5	0.4
$N_K, N_L = 16, 0$	0.0034939	0.00001835	6.0	0.5	0.4
$N_K, N_L = 12, 6$	0.0030207	0.00001442	8.8	1.3	1.3
$N_K, N_L = 12, 12$	0.0025098	0.00001015	11.0	3.1	2.1

zero velocity on the top and bottom, and periodicity in x- and z-directions. Initially a spherical drop is centered at (0.5, 0.5), with radius $R_0 = 0.125$ ($\Delta x = \Delta y = \Delta z = R_0/22$) and surface tension $\sigma = 0.357$. Both fluids have equal density, $\rho_L = \rho_G = 4$, and viscosity, $\mu_L = \mu_G = 1$. The initial velocity field is zero. The exact solution is zero velocity for all time. In this situation the relevant parameter is the Ohnesorge number $Oh = (\mu^2/\sigma\rho R_0)^{1/2} \sim 0.237$.

Table 1 reports the ℓ_∞ and ℓ_1 norms of the spurious velocities and the errors for the pressure jump. According to previous studies (see [22,32,48]), the value of the spurious currents are expected to be of order $0.01\sigma/\mu \sim 0.00357$. This order of magnitude is also confirmed by our calculations. The magnitude of the spurious currents are in agreement with the values calculated by the SURFER code using the CSF and CSS methods. The PROST method developed by Renardy and Renardy [48] appears to be a very interesting method since it reduces by two orders of magnitude the spurious velocities. Note that [22] have developed the Sharp Surface tension Force (SSF) method that significantly reduces the spurious currents compared to CSF methods. Table 1 also indicates that for this case the magnitude of the spurious velocities is decreasing with the increase of the number of filtering N_K while it is nearly independent of the value of N_L . The error in the pressure jump is nearly constant for the different filtering considered for $N_L = 0$. We observe that the errors are increasing with increasing N_L while the spurious currents are decreased. The value of ΔP_0 is found to be very close to the exact value while the value of ΔP_{total} is found to be around 6% lower than the exact pressure. The errors $E_{partial}$ and E_0 have similar magnitude, less than the magnitude of the error E_{total} . Consequently, the error measured by E_{total} is mainly due to the pressure evolution across the diffused interface.

Finally, this test case shows that our method gives spurious velocities which are close to the magnitude given by the CSF and CSS methods implemented in the SURFER code.

4.2. Circular drop at equilibrium

The second test is a 2D simulation based on the previous test case. The drop is a disc of radius $R_0 = 0.125$ centered in a square of dimension $L_x \times L_y = 1 \times 1$. The calculations are performed with the same grid spacing $\Delta x = \Delta y = L_x/96 = R_0/22$ and the same time step ($\Delta t = 10^{-5}$). The number of time steps is now $N_t = 20,000$ in order to obtain convergence for the magnitude of the spurious currents. The boundary conditions are zero velocity on the frontiers of the computational domain. The converged values of the spurious velocities are reported in Table 2. The cost of the smoothing procedure used to reduce the effect of the spurious currents is also reported in Table 2. It is evaluated by calculating the relative difference $C_{CPU} = (t_{N_K, N_L} - t_{0,0})/t_{0,0}$, where t_{N_K, N_L} is the CPU time for a simulation using N_K and N_L iterations.

For $N_K = N_L = 0$ we observe larger spurious velocity but the drop centre remains immobile and its shape remains nearly spherical. This is also verified up to 80,000 time steps for this case. We can observe that the introduction of the filtering reduces the spurious velocities. The trends observed for the previous 3D test are also confirmed by these 2D simulations. The same order of magnitude is found for the spurious velocities and their converged maximum magnitude can be estimated using:

Table 2

Norms of velocity and pressure jumps at $N_t = 20000^{th}$ time step ($\Delta t = 10^{-5}$). $\rho_L = \rho_G = 4$, $\mu_L = \mu_G = 1$ and $\sigma = 0.357$.

Filtering	ℓ_∞	ℓ_1	E_{total} (%)	$E_{partial}$ (%)	E_0 (%)	C_{CPU}
$N_K, N_L = 0, 0$	0.0054703	0.00023591	10.1	8.5	8.7	1
$N_K, N_L = 6, 0$	0.0021841	0.00019679	5.2	2.1	1.9	1.0029
$N_K, N_L = 12, 0$	0.0014175	0.00014107	4.2	0.8	0.7	1.0061
$N_K, N_L = 16, 0$	0.0012164	0.00011994	3.8	0.4	0.3	1.0079
$N_K, N_L = 12, 6$	0.0010234	0.000083260	6.6	2.7	0.6	1.0090
$N_K, N_L = 12, 12$	0.00081147	0.000043934	8.7	4.3	1.7	1.0122

$$\ell_\infty \approx 0.004\sigma/\mu \quad (30)$$

which gives $\ell_\infty \sim 0.0015$. The effect of the number of smoothing steps is found to have more effect on the converged 2D values. We clearly observe that the magnitude of the spurious velocities is reduced with the increase of both N_κ and N_L . This tendency is also observed for the precision of the pressure jump that is improved with increasing N_κ . The effect of N_L is clearly to reduce the precision for the pressure but its effect is not perceptible for $N_L \leq 6$. For this test case, the recommended chose is obtained for $N_\kappa \approx 12$ and $N_L \approx 6$ to optimize both the reduction of spurious currents and the pressure jump precision.

The CPU cost reported in Table 2 indicates that the smoothing procedure is not expensive. The relative additional cost can be estimated by $C_{CPU} \approx 1 + 0.0005(N_\kappa + N_L)$. Note that this evolution has been confirmed by doing additional simulations for larger value of N_κ and N_L , typically of order 100.

4.3. Circular drop at equilibrium for liquid/gas system

The third test case is for fluid properties and dimensions also considered in the rest of the paper, i.e. millimetric liquid drops in a gas. For this test, the surface tension is $\sigma = 0.072$ N/m, the viscosity and density are $\mu_L = 10^{-2}$ Pa s, $\mu_G = 10^{-5}$ Pa s, $\rho_L = 10^3$ kg/m³ and $\rho_G = 1$ kg/m³ so that the viscosity and density ratio are, respectively $\mu_L/\mu_G = 10^3$ and $\rho_L/\rho_G = 10^3$. A circular drop of radius $R_0 = 1$ mm is centered in the domain. The corresponding Ohnesorge number is $Oh = (\mu^2/\sigma\rho R_0)^{1/2} \sim 0.0037$. The size of the computational domain is $L_x \times L_y = 4 \times 4$ mm². The boundary conditions and the initial condition are kept unchanged, a zero velocity being imposed on the boundaries. Different grids with uniform spacing are considered: $\Delta x = \Delta y = L_x/96 = R_0/24$, $\Delta x = \Delta y = L_x/144 = R_0/36$, $\Delta x = \Delta y = L_x/192 = R_0/48$ and $\Delta x = \Delta y = L_x/288 = R_0/72$. Different time steps are also tested: $\Delta t = 10^{-5}$ s, $\Delta t = 5 \times 10^{-6}$ s, $\Delta t = 10^{-6}$ s and $\Delta t = 10^{-7}$ s.

Table 3 gives the effect of the filtering on the ℓ_∞ and the ℓ_1 norms of the spurious velocities and on the error for the jump in pressure for $\Delta x = \Delta y = L_x/96 = R_0/24$ and $\Delta t = 10^{-6}$ s. The number of time steps is $N_t = 20,000$ in order to obtain the convergence of the simulations. For $N_\kappa = N_L = 0$, we observe the deformation of the drop and its migration due to the amplification of the spurious velocities for $N_t > 20,000$. The introduction of the filtering stabilizes the calculation. The magnitude of the spurious currents are found to be correctly estimated by the correlation (30) $\ell_\infty \approx 0.004\sigma/\mu \sim 0.029$. Concerning the effect of the successive filtering, the tendencies observed for the previous 2D test case are also confirmed. E_0 and E_{partial} have very close values smaller than E_{total} . Fig. 4 presents the pressure profile versus the coordinate x at the position $y = 2$ mm corresponding to the position of the drop center. The effect of N_κ is presented in Fig. 4(a) for $N_L = 0$ while Fig. 4(b) reports the effect of N_L for $N_\kappa = 12$. We observe that an increase of successive smoothing tends to increase the size of the numerical transition for the pressure across the interface, resulting in an increase of the pressure inside the drop.

Table 4 reports the effect of the grid spacing for $\Delta t = 10^{-6}$ s and $N_\kappa, N_L = 12, 6$. We observe that the order of magnitude of the spurious currents is not significantly different between the less refined grid $\Delta x = \Delta y = L/48 = R_0/12$ and the more refined grid $\Delta x = \Delta y = L/288 = R_0/72$. The values of the spurious currents are slightly decreased when the number of cells per radius is increased. The evolution of the error E_{total} versus the grid spacing clearly indicates a precision close to first order. The error E_0 based on the value of the pressure at the drop center is found to be close to second-order, in agreement with the spatial discretization used in the code. This difference between E_0 and E_{total} seems to be due to the procedure used to solve the interface (see also [8] who observed a similar trend for rising bubbles in a liquid at rest).

Table 5 shows the effect of the time step for $\Delta x = \Delta y = L/96 = R_0/24$ and $N_\kappa, N_L = 12, 6$. The number of time steps N_t reported in Table 5 is chosen so that the total time simulated is the same for the four cases, the time steps varying from $\Delta t = 10^{-7}$ s to $\Delta t = 10^{-5}$ s. We observe that the value of the time step has a very small effect on the magnitude of the spurious currents. Their magnitude is slowly increasing with the decrease of the time step, certainly resulting from the increase of the number of iterations used to calculate the solution at the same final time.

4.4. Circular cap drop at equilibrium wetting a plane surface for liquid/gas system

The last test case considers a drop wetting a surface for different values of the contact angle. We consider different situations from a wetting surface $\theta_s = 10^\circ$ to a non wetting surface $\theta_s = 170^\circ$. The volume of the drop πR_0^2 is the same for all

Table 3

Effect of the capillary filtering on the converged norms of the spurious velocity and the pressure jump for $\Delta x = \Delta y = L/96 = R_0/24$ and $\Delta t = 10^{-6}$ s ($N_t = 20000$). $\mu_L = 10^{-2}$ Pa s, $\mu_G = 10^{-5}$ Pa s, $\rho_L = 10^3$ kg/m³, $\rho_G = 1$ kg/m³ and $\sigma = 0.072$ N/m.

Filtering	ℓ_∞	ℓ_1	E_{total} (%)	E_{partial} (%)	E_0 (%)
$N_\kappa, N_L = 0, 0$	–	–	–	–	–
$N_\kappa, N_L = 6, 0$	0.036821	0.0061711	5.4	2.7	2.6
$N_\kappa, N_L = 12, 0$	0.026275	0.0042933	4.3	1.3	1.3
$N_\kappa, N_L = 16, 0$	0.027352	0.0040360	3.9	0.9	0.9
$N_\kappa, N_L = 12, 6$	0.036574	0.0072896	3.9	0.7	2.4
$N_\kappa, N_L = 12, 12$	0.038688	0.0076322	4.1	0.1	4.8

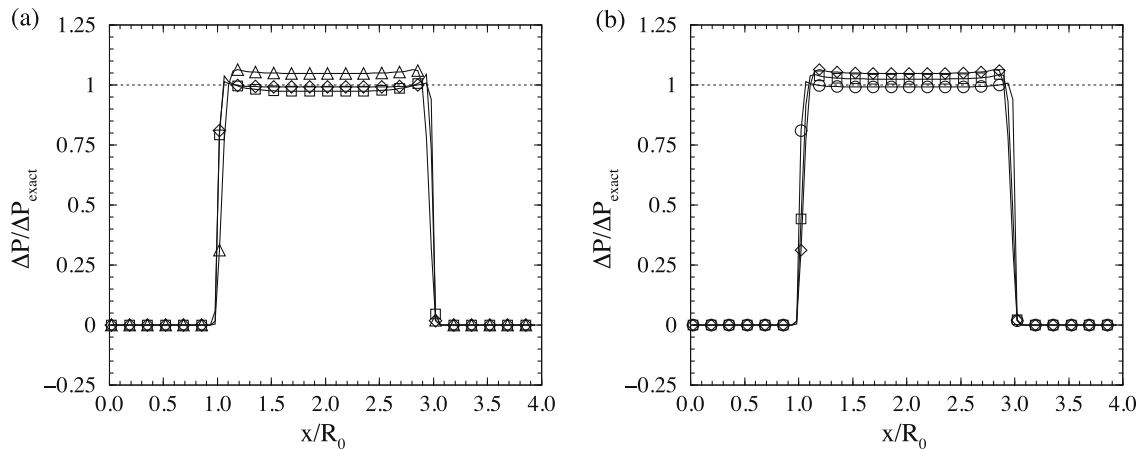


Fig. 4. Evolution of pressure normalized by $\Delta P_{\text{exact}} = \sigma/R_0$ versus x/R_0 for $y = 2$ mm. $\Delta x = \Delta y = L/96 = R_0/24$ and $\Delta t = 10^{-6}$ s ($N_t = 20,000$). $\mu_L = 10^{-2}$ Pa s, $\mu_G = 10^{-5}$ Pa s, $\rho_L = 10^3$ kg/m³ and $\rho_L = 1$ kg/m³. (a) Effect of N_K for $N_L = 0$: \square $N_K = 6$, \diamond $N_K = 12$ and \triangle $N_K = 16$. (b) Effect of N_L for $N_K = 12$: \circ $N_L = 0$, \square $N_L = 6$ and \diamond $N_L = 12$.

Table 4

Effect of the grid spacing on the converged norms of the spurious velocity and the pressure jump for $N_K, N_L = 12, 6$ and $\Delta t = 10^{-6}$ s ($N_t = 20,000$). $\mu_L = 10^{-2}$ Pa s, $\mu_G = 10^{-5}$ Pa s, $\rho_L = 10^3$ kg/m³ and $\rho_L = 1$ kg/m³.

Grid spacing	ℓ_∞	ℓ_1	$E_{\text{total}} (\%)$	$E_0 (\%)$
$\Delta x = \Delta y = L/48 = R_0/12$	0.062761	0.012896	6.6	6.9
$\Delta x = \Delta y = L/96 = R_0/24$	0.036574	0.0072896	3.9	2.4
$\Delta x = \Delta y = L/144 = R_0/36$	0.027781	0.0049319	3.0	1.3
$\Delta x = \Delta y = L/192 = R_0/48$	0.022240	0.0040500	2.7	0.8
$\Delta x = \Delta y = L/288 = R_0/72$	0.018444	0.0033273	2.1	0.3

Table 5

Effect of the time step on the norms of the spurious velocity and the pressure jump for $N_K, N_L = 12, 6$ and $\Delta x = \Delta y = L/96 = R_0/24$. $\mu_L = 10^{-2}$ Pa s, $\mu_G = 10^{-5}$ Pa s, $\rho_L = 10^3$ kg/m³ and $\rho_L = 1$ kg/m³.

Time step	ℓ_∞	ℓ_1	$E_{\text{total}} (\%)$	$E_0 (\%)$
$\Delta t = 10^{-5}$ s ($N_t = 2000$)	0.032466	0.0063115	3.8	2.3
$\Delta t = 5 \times 10^{-6}$ s ($N_t = 4000$)	0.034474	0.0068387	3.8	2.4
$\Delta t = 10^{-6}$ s ($N_t = 20,000$)	0.036574	0.0072896	3.9	2.4
$\Delta t = 10^{-7}$ s ($N_t = 200,000$)	0.036993	0.0073866	3.9	2.5

cases and corresponds to a disc of radius $R_0 = 1$ mm. Hence, the radius R of the circular cap that satisfies the contact angle θ_S with the wall and the jump in pressure ΔP are given by

$$R = R_0 \sqrt{\frac{\pi}{\theta_S - \sin \theta_S \cos \theta_S}}, \quad \Delta P = \frac{\sigma}{R}$$

These conditions are imposed as initial conditions so that the exact solution is zero velocity for all time. The dimension of the numerical domain is $L_x \times L_y$ where L_x is twice the drop width ($L_x = 4R \sin \theta_S$ for $\theta_S \leq 90^\circ$ and $L_x = 4R$ otherwise) and $L_y = 2R(1 - \cos \theta_S)$ is twice the drop height. The size of the grid spacing is defined so that the drop height corresponds to 40 cells. The time step, the number of time steps and the number of iterations for the capillary filtering are $\Delta t = 10^{-6}$ s, $N_t = 20,000$ and $N_K, N_L = 12, 6$, respectively.

Table 6 reports the value of the ℓ_∞ and ℓ_1 norms and the values of the errors E_{total} , E_{partial} and E_0 . We observe that the order of magnitude of the spurious currents are not significantly changed compared to the isolated drop. Their maximum value can be estimated by relation (30) obtained in unbounded situations ($\ell_\infty \approx 0.004\sigma/\mu \sim 0.029$). We do not observe a significant effect of the procedure used to impose the contact angle on the development of spurious velocities. It can be seen that their magnitude seems to increase with the increase of the value of the contact angle due to the increase of the drop curvature. Considering the pressure jump we observe the opposite evolution: the error increases when the contact angle decreases. For $\theta = 10^\circ$ a particular behavior is observed since the error E_0 has comparable value compared with the other angles (around

Table 6

Norms of velocity and pressure jumps at $N_{tps} = 20,000$ th time step ($\Delta t = 10^{-6}$ s) for $N_\kappa, N_L = 12, 6$ and $\Delta x = \Delta y = L/192 = R_0/48$. $\mu_L = 10^{-2}$ Pa s, $\mu_G = 10^{-5}$ Pa s, $\rho_L = 10^3$ kg/m³ and $\rho_L = 1$ kg/m³.

Contact angle	ℓ_∞	ℓ_1	E_{total} (%)	$E_{partial}$ (%)	E_0 (%)
$\theta = 10^\circ$	0.017	0.0011	15	13	4.2
$\theta = 30^\circ$	0.023	0.0032	5.8	5.1	3.8
$\theta = 60^\circ$	0.026	0.0035	3.4	3.6	3.2
$\theta = 90^\circ$	0.039	0.0066	4.5	0.4	1.5
$\theta = 120^\circ$	0.050	0.0078	6.9	2.8	0.96
$\theta = 150^\circ$	0.068	0.0088	7.1	3.2	1.3
$\theta = 170^\circ$	0.085	0.011	7.4	3.4	1.6

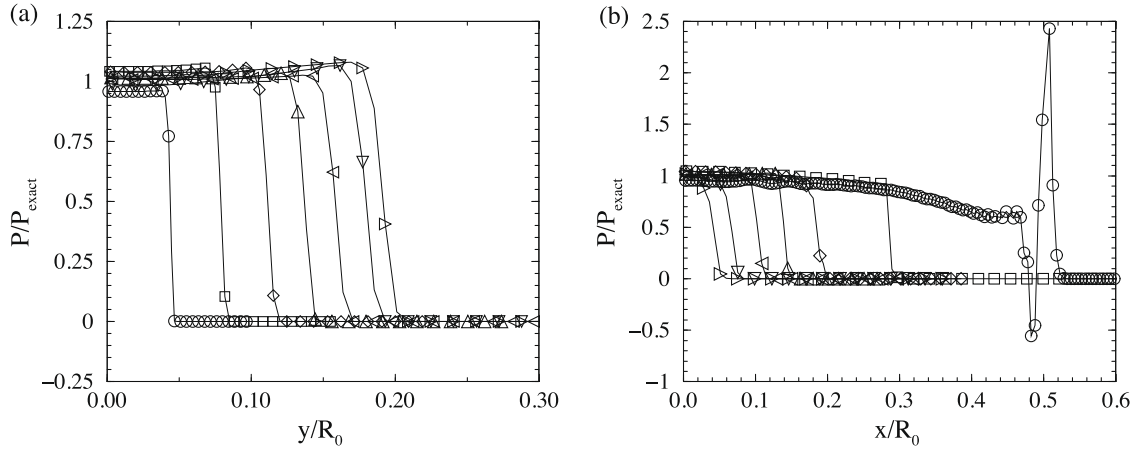


Fig. 5. Pressure profiles normalized by σ/R for different contact angles. $\circ \theta_S = 10^\circ$, $\square \theta_S = 30^\circ$, $\diamond \theta_S = 60^\circ$, $\triangle \theta_S = 90^\circ$, $\triangleleft \theta_S = 120^\circ$, $\nabla \theta_S = 150^\circ$ and $\triangleright \theta_S = 170^\circ$. (a) Pressure profile normal to the wall at the drop center ($x = 0$). (b) Pressure distribution on the wall ($y = 0$).

some percents) while E_{total} and $E_{partial}$ have much bigger values around 15%. The explanation is given by the pressure profiles inside the drop.

The pressure profile in the y -direction perpendicular to the wall at the drop center ($x = 0$) and the pressure distribution on the wall ($y = 0$) are reported in Fig. 5. We observe that the pressure profile is very close to the exact solution for all the angles except for $\theta = 10^\circ$. For this angle the normal profile presents a satisfactory evolution while the wall profile is not uniform near the contact angle. We have changed the number of filtering N_κ and N_L but for $\theta = 10^\circ$ the amplitude of the spatial oscillations do not significantly vary. This pressure profile is also stable in time, the simulation has been run until $N_t = 200,000$ time steps. This particular behavior of the pressure at the vicinity of the contact line only appears at small contact angle. An implicit treatment of (20) is a possible improvement to reduce the spatial oscillation of the pressure.

5. Equilibrium shape of a drop released on a wall

In this section, we consider some validations of the implementation of the static angle in bidimensional (plane) configurations. For the simulations reported in this section the contact angle is imposed to be constant and equal to the static angle θ_S . We consider the shape at equilibrium of a drop released on a horizontal wall. The drop is initially a semicircle and the initial contact angle with the wall is equal to 90° (Fig. 6(a)). If the contact angle θ_S is different from the initial angle, the contact line moves and the drop deforms to respect the contact angle θ_S . The drop is also flattened due to gravity. Considering the density ratio between the liquid and the surrounding gas, the final shape of the drop depends on two parameters, namely the static angle θ_S and the Eotvos number $Eo = \rho_L g R_0^2 / \sigma$ based on the initial radius R_0 , the liquid density ρ_L , the gravity g and the surface tension σ .

5.1. Absence of gravity ($Eo = 0$)

The main interest of the simplified situation $Eo = 0$ is that the static shape of the drop is a circular cap that respects the contact angle θ_S with the wall (Fig. 6(b)). By conservation of the volume of the drop, it is possible to geometrically calculate at equilibrium the radius of the circle R , the length of spreading L , the height of the drop e and the pressure difference ΔP between the drop and the surrounding gas:

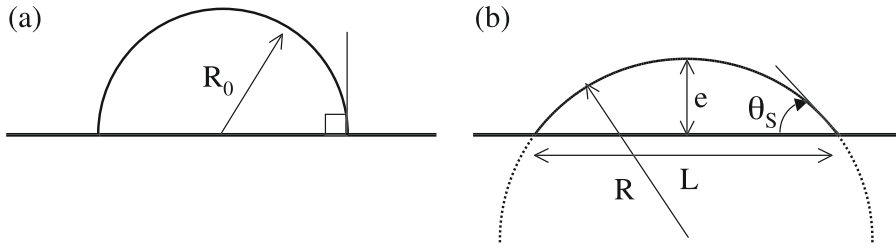


Fig. 6. (a) Initial shape of the drop released on the wall. (b) Definition of the characteristic parameters for the final shape for $Eo = 0$.

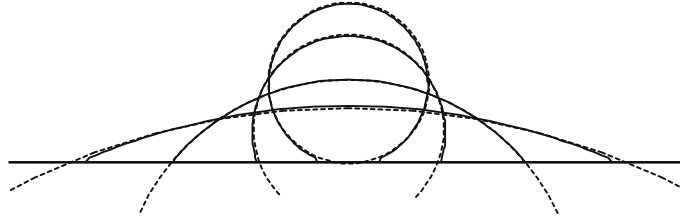


Fig. 7. Final drop shape for $\theta_S = 20^\circ, \theta_S = 50^\circ, \theta_S = 110^\circ$ and $\theta_S = 170^\circ$. Dashed lines: theoretical shape. Continuous line: numerical simulations ($C = 0.5$) for $\Delta x = \Delta y = R_0/40$ and $N_K = N_L = 16$.

$$R = R_0 \sqrt{\frac{\pi}{2(\theta_S - \sin\theta_S \cos\theta_S)}}, \quad L = 2R \sin\theta_S, \quad e = R(1 - \cos\theta_S) \\ \Delta P = \sigma/R \quad (31)$$

The numerical domain is a regular grid in the Cartesian coordinates (x, y) with $-3R_0 \leq x \leq 3R_0$ and $0 \leq y \leq 2R_0$, x and y being parallel and normal to the wall, respectively. Forty cells describe the initial radius R_0 of the drop ($\Delta x = \Delta y = R_0/40$). The time step is $\Delta t = 1.5 \times 10^{-4}$ s. After being released on the wall with its initial shape (Fig. 6(a)) a drop oscillates until it reaches its final shape. Some comparisons with the theoretical shape are reported in Fig. 7 for different contact angles ($\theta_S = 20^\circ, \theta_S = 50^\circ, \theta_S = 110^\circ, \theta_S = 170^\circ$) and the following physical parameters: $R_0 = 0.01$ m, $\rho_l = 1000$ kg m $^{-3}$ and $\mu_l = 10^{-2}$ Pa s for the liquid, $\rho_g = 1$ kg m $^{-3}$ and $\mu_g = 10^{-5}$ Pa s for the gas and $\sigma = 0.072$ N m $^{-1}$. Note that for $\theta_S = 170^\circ$ the initial impulse generated by the discontinuity of the contact angle generates the drop detachment from the wall. For this situation, the initial condition is the equilibrium situation obtained for $\theta_S = 130^\circ$. For all the contact angles θ_S , the comparison is qualitatively very satisfactory with the theoretical shape given by (31). This is confirmed by the mean difference between the numerical solution and the theoretical prediction defined by:

$$E = \frac{1}{N} \sum_{k=1}^N \frac{|x_k^{C=0.5} - x^{th}|}{R} \quad (32)$$

where N is the number of nodes discretizing the interface located at $x_k^{C=0.5}$, $y_k^{C=0.5}$ is the corresponding position of the interface and x^{th} is the theoretical x -coordinate of the interface at $y_k^{C=0.5}$. For the shapes reported in Fig. 7, the mean difference is 1.7%, 0.3%, 2% and 2.2% for $\theta_S = 20^\circ, \theta_S = 50^\circ, \theta_S = 110^\circ$ and $\theta_S = 170^\circ$, respectively.

Fig. 8 reports the numerical values of the length of spreading L , the drop height e and the pressure jump ΔP_{total} , $\Delta P_{partial}$ and ΔP_0 versus the contact angle θ_S . As suggested by the shape reported in Fig. 7, the comparison with the theoretical expression is found to be very satisfactory for both hydrophobic and hydrophilic situations. The best precision is obviously observed for $\theta_S = 90^\circ$ because the drop remains immobile and there is no displacement of the contact line. The best description of the pressure jump evolution is given by $\Delta P_{partial}$ and ΔP_0 . As previously observed, this figure illustrates the loss in precision at low and large contact angles. For $\theta_S = 10^\circ$, the pressure distribution is non uniform near the contact line (see Section 4.4) and induces significant errors in the drop shape and the pressure jump.

5.2. Spreading effect due to gravity

We consider the effect of gravity on the shape of the drop. Due to the combination of gravity that spreads the drop and surface tension that maintains its sphericity, the drop shape evolves in order to also satisfy the contact angle at the wall. We define the thickness e of the drop as the maximum vertical distance between the wall and the interface. For $Eo \ll 1$, the prob-

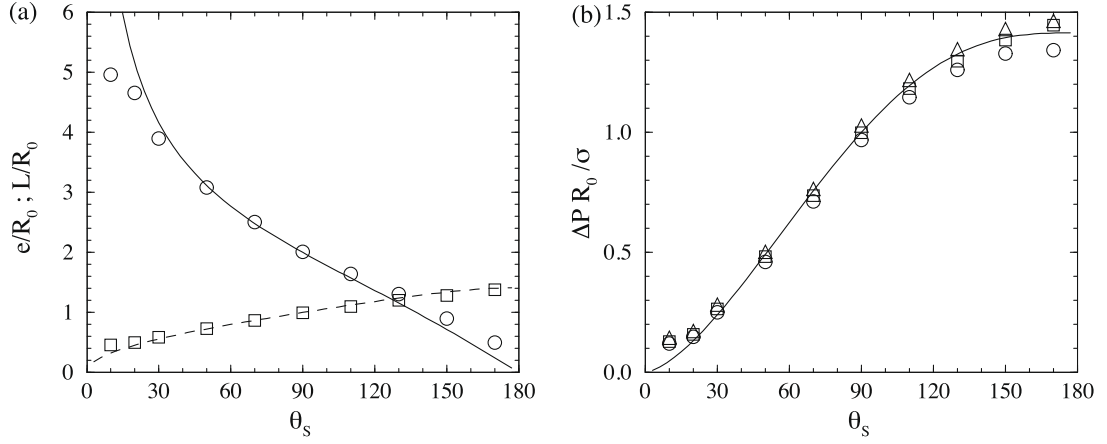


Fig. 8. (a) Geometrical characteristic of the drop versus the contact angle θ_s , \circ length of spreading L and \square drop height e . (b) Pressure inside the drop P versus the contact angle θ_s , \circ ΔP_{total} , \square $\Delta P_{partial}$ and \triangle ΔP_0 . — theoretical solutions given by (31).

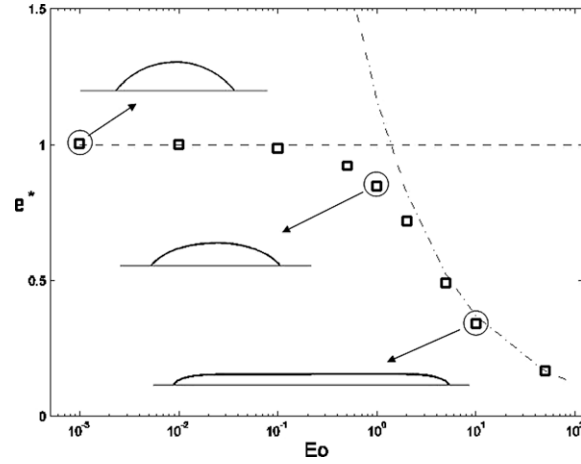


Fig. 9. Normalized thickness $e^* = e/e_0$ of a drop at rest on a hydrophilic wall ($\theta_s = 50^\circ$). \square : numerical simulations, — — Eq. (33), — . — Eq. (34).

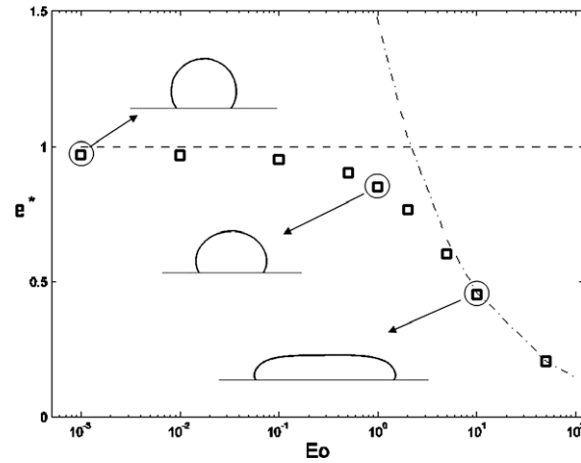


Fig. 10. Normalized thickness $e^* = e/e_0$ of a drop at rest on a hydrophilic wall ($\theta_s = 130^\circ$). \square : numerical simulations, — — Eq. (33), — . — Eq. (34).

lem is controlled by the surface tension and the drop is a circular cap with angle θ_s . The thickness of the drop deduced from (31) is then:

$$e_0 = R_0(1 - \cos\theta_s) \sqrt{\frac{\pi}{2(\theta_s - \sin\theta_s \cos\theta_s)}} \quad (33)$$

For $Eo \gg 1$, the drop spreads under the gravity effect and forms a puddle whose thickness is directly proportional to the capillary length:

$$e_\infty = 2 \sqrt{\frac{\sigma}{\rho_l g}} \sin\left(\frac{\theta_s}{2}\right) \quad (34)$$

The shape of the drop is computed for a large range of Eotvos numbers varying from situations controlled by surface tension ($Eo = 0.001$) to situations controlled by gravity ($Eo = 50$). The simulations are carried out using $\Delta x = \Delta y = R_0/40$ and $N_\kappa = N_l = 16$. The time step is $\Delta t = 1.5 \times 10^{-4}$ s. The evolution of the thickness of the drop is plotted versus the Eotvos number in Fig. 9 for a hydrophilic wall ($\theta_s = 50^\circ$) and in Fig. 10 for a hydrophobic wall ($\theta_s = 130^\circ$). The simulations are found to be in very good agreement with the two asymptotic solutions (33) and (34). As expected the transition between the circular cap and the puddle is observed to occur around $Eo = 1$ when gravity and surface tension effects are of same order of magnitude.

6. Partial wetting dynamics

The objective of this section is to test the method for moving contact lines. For this purpose we consider the axisymmetric spreading of a droplet for a partially wetting liquid. Some preliminary tests have been performed in order to investigate the convergence of the results with the spatial and time refinement. The simulations are compared with the experiments of [33].

6.1. Statment of the problem

The problem considered consists in measuring the spreading of a drop initially placed on a wall (Fig. 11). For complete wetting conditions [39] showed that their experimental measurement of the dimensionless drop base area A can be well correlated by a power law $A = K\tau^n$ where $\tau = t\sigma/\mu V^{1/3}$ is the dimensionless time using the drop volume V . The theoretically predicted values and experimental measurement of the power n are within the range of $0.2 - 0.29$ [33]. For partially wetting liquids [59] has shown using different fluids that the dimensionless time τ is also the pertinent time to describe the spreading of the drop with $n \simeq 0.28$. Lavi and Marmur [33] performed experiments for different liquids partially wetting a coated silicon wafer. They represented their experimental data by:

$$\frac{A}{A_f} = 1 - \exp\left(-\frac{K}{A_f} \tau^n\right) \quad (35)$$

where A_f is the final, equilibrium value of the wet (solid–liquid) area. Note that this representation of the data reduces to the previous power law for complete wetting in the limit of complete wetting, where the final wet area at equilibrium is infinite ($A_f \rightarrow \infty$).

Numerical axisymmetric simulations are compared with three experiments of [33]. The corresponding physical properties are given in Table 7. We consider a drop of radius $R_0 = (3V/4\pi)^{1/3} = 1$ mm initially placed on a wall. We numerically impose an initial surface of contact A_0 corresponding to a drop center located at the distance $0.95R_0$ from the wall. The corresponding initial contact angle is thus $\theta_d(0) \approx 162^\circ$.

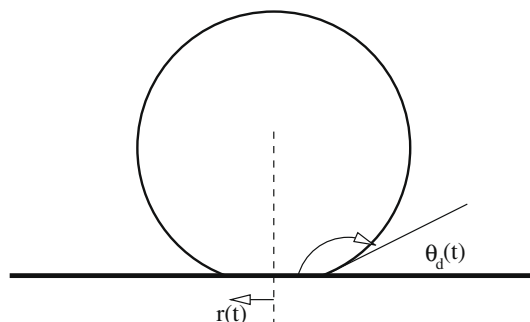
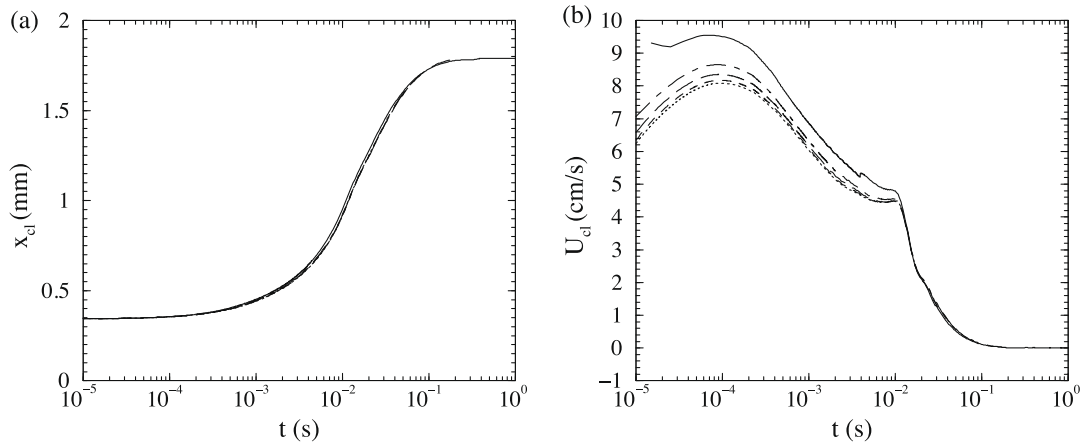


Fig. 11. Initial condition.

Table 7Physical properties and experimental values for K and n from [33].

Case	ρ_L (kg/m ³)	μ_L (Pa s)	σ (N/m)	θ_5	La	K	n
LM2	773	3.07×10^{-3}	0.027	35.9°	2210	0.866	0.736
LM3	809	34.0×10^{-3}	0.032	41.5°	20	0.471	0.699
LM5	974	62.2×10^{-3}	0.041	54.2°	10	0.352	0.775

**Fig. 12.** Effect of the time step on the spreading for case LM3 using a no-slip condition ($\lambda = 0$). (a) Contact line position x_{cl} . (b) Contact line velocity U_{cl} . — $\Delta t = 5 \times 10^{-6}$ s, - - - $\Delta t = 2 \times 10^{-6}$ s, - · - $\Delta t = 10^{-6}$ s, - - - $\Delta t = 4 \times 10^{-7}$ s, - - - $\Delta t = 10^{-7}$ s.

6.2. Preliminary tests

Some preliminary tests are presented in this section in order to determine the grid refinement and the time step used for the comparison with experiments. In order to characterize the effect of the grid refinement, the grid size is reduced in the vicinity of the wall. A geometrical progression makes the connection with a regular grid where $\Delta = \Delta x = \Delta y = R_0/50 = 20 \mu\text{m}$. The size of the refined zone is $R_0/5$ and three different refined grids are compared with the regular grid called $GRID_1$. Grid refinement at the wall are $\Delta_2 = \Delta/2 = R_0/100 = 10 \mu\text{m}$ ($GRID_2$), $\Delta_5 = \Delta/5 = R_0/250 = 4 \mu\text{m}$ ($GRID_5$) and $\Delta_{10} = \Delta/10 = R_0/500 = 1 \mu\text{m}$ ($GRID_{10}$), respectively. Typically, the grid spacing has been divided by 2, 5 and 10 near the wall. The index used in the name of the grid indicates the grid refinement relative to the regular grid. The connection with the regular part of the grid where $\Delta x = \Delta y = R_0/50$ has been made so that the ratio between two successive cells is less than 1.1. The number of nodes used to describe the refinement zone are 15, 20 and 25 for $GRID_2$, $GRID_5$ and $GRID_{10}$, respectively.

The effect of the time step is presented for the regular grid $GRID_1$ and a no-slip condition at the wall ($\lambda = 0$). The case LM3 is considered. Fig. 12 presents the evolution of the drop spreading obtained for different time steps: $\Delta t = 5 \times 10^{-6}$ s, $\Delta t = 2 \times 10^{-6}$ s, $\Delta t = 10^{-6}$ s, $\Delta t = 4 \times 10^{-7}$ s and $\Delta t = 10^{-7}$ s. Fig. 12(a) and (b) report the time evolution of the contact line position x_{cl} and the contact line velocity U_{cl} , respectively. The evolution of the contact line is found to converge with the time step, the main effect being observed on the evolution of the velocity. The maximum difference is observed at approximately $t \approx 10^{-4}$ s and the maximum values are respectively 9.55 cm/s, 8.67 cm/s, 8.35 cm/s, 8.17 cm/s and 8.08 cm/s. As shown in Fig. 12(a), the effect is small on the wetted area since the velocities are very close for time $t > 2 \times 10^{-2}$.

The effect of the mesh refinement on the drop spreading is reported in Fig. 13 for the case LM3 using a no-slip condition ($\lambda = 0$). The time step used for the computation is $\Delta t = 10^{-7}$ s. We observe in Fig. 13 that the refinement does not change significantly the shape of the time evolutions. Fig. 13(a) shows an acceptable convergence with the grid spacing for the contact line position x_{cl} . The curves are translated to the right with increasing the refinement indicating a reduction of the spreading velocity with the refinement. This velocity reduction is observed at the beginning of the spreading, the evolutions being independent on the grid spacing for $t > 2 \times 10^{-2}$ (see Fig. 13(b)). The spreading is generated by the initial impulse transmitted to the drop due to the initial imbalance at the contact line. The velocity reaches a maximum just after the beginning of the spreading around $t \approx 10^{-4}$ s and then decreases until the stabilization of the drop. Fig. 13(b) clearly shows that the grid convergence is not satisfactory when the velocity evolution is considered. Indeed, the grid convergence cannot be achieved using a no-slip condition due to the increase of the wall shear rate with mesh refinement [2].

Fig. 14 presents the effect of refinement when the Navier slip condition is imposed using the slip length $\lambda = 0.01R_0$. The selected slip length corresponds to $\Delta/2$. A time convergence study has first been performed for the four grids in order to determine the time step to be used for the comparison. The corresponding time steps are from the less refined to the more refined grid $\Delta t = 10^{-7}$ s, $\Delta t = 10^{-7}$ s, $\Delta t = 0.5 \times 10^{-7}$ s and $\Delta t = 0.2 \times 10^{-7}$ s. The figure shows that for the four grids the

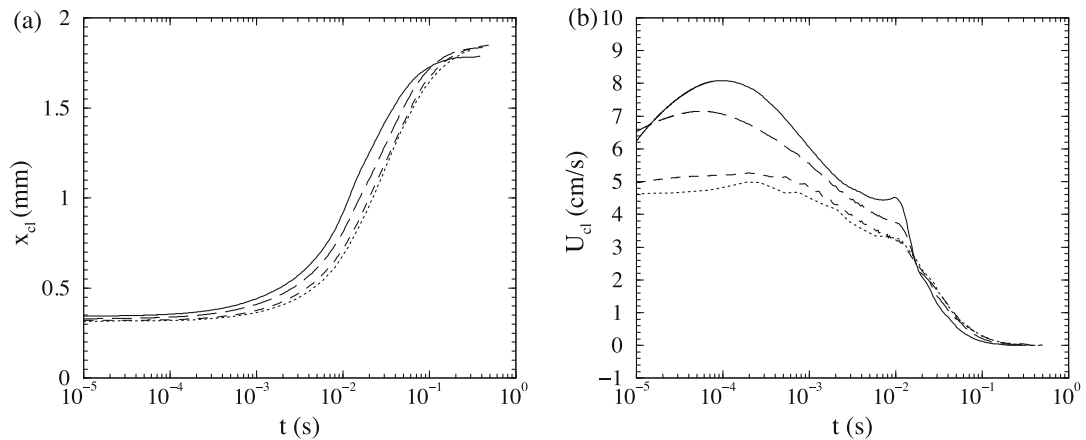


Fig. 13. Effect of grid refinement on the spreading for case LM3 using a no-slip condition ($\lambda = 0$). — Δ_1 , --- Δ_2 , - - - Δ_5 , ... Δ_{10} . (a) Contact line position x_{cl} . (b) Contact line velocity U_{cl} .

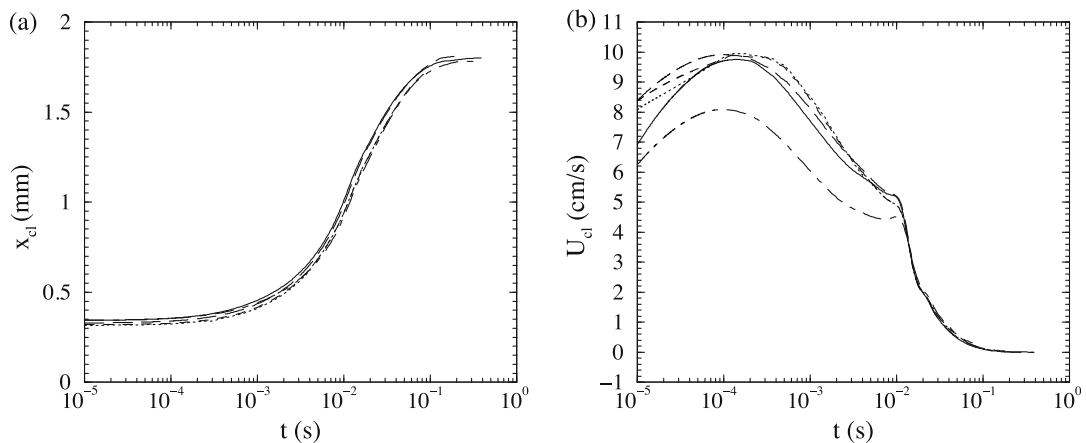


Fig. 14. Effect of grid refinement on the spreading for case LM3 using the slip length $\lambda = 0.01R_0$. — Δ_1 , --- Δ_2 , - - - Δ_5 , ... Δ_{10} . - - - - - No-slip condition $\lambda = 0$. (a) Contact line position x_{cl} . (b) Contact line velocity U_{cl} .

difference is not perceptible for the contact line position x_{cl} . Again difference between cases are revealed by comparing the velocity of the contact line. The grid convergence is very satisfactory when a slip length is used. For comparison, the evolution obtained for the less refined grid $GRID_1$ with a no-slip condition ($\lambda = 0$) and $\Delta t = 10^{-7}$ s is reported. Volume fraction being advected by cell face normal velocities, the contact line velocity is the velocity calculated at the intermediate length scale $\Delta/2$ when a no-slip condition is imposed. For $GRID_1$, this distance ($0.01R_0$) corresponds to the slip length imposed in the simulations. The comparison shows that, strictly speaking, a no-slip condition $\lambda = 0$ with a grid size Δ is not equivalent to a slip condition with the slip length $\lambda = \Delta/2$. The slip length λ is an input parameter in the method proposed here. As shown by Spelt [55] and Afkhami et al. [2], the results for a given value of λ appear to be convergent with respect to the grid spacing when the slip length is resolved. The objective of this section is not a discussion about the optimal value of the slip length for the simulation (see [55]). As shown in Fig. 14(a), the difference between $\lambda = 0$ and $\lambda = 0.01R_0$ is not noticeable when considering the contact line position evolution for the physical problem considered here. The value $\lambda = 0.01R_0$ has been used for the comparison with experiments reported below.

6.3. Comparison with experiments

In this section, simulations are compared with the experiments of [33] that report the time evolution of the contact line. The physical properties are reported in Table 7 for the cases LM2, LM3 and LM5. The simulations reported in this section are performed using $\Delta t = 10^{-7}$ s and $\lambda = 0.01R_0$. The grid is the uniform grid $GRID_1$ ($\Delta = R_0/50$). Fig. 15 reports the time evolution of the dimensionless wetted area $A^* = (A - A_0)/(A_f - A_0)$. The agreement with experiments is found to be very satisfactory for the two cases LM3 and LM5 while a significant difference is observed for the case LM2. For LM2, the spreading is found to be slower at short time, faster at larger time and characterized by oscillations at the end of the spreading. In order to make

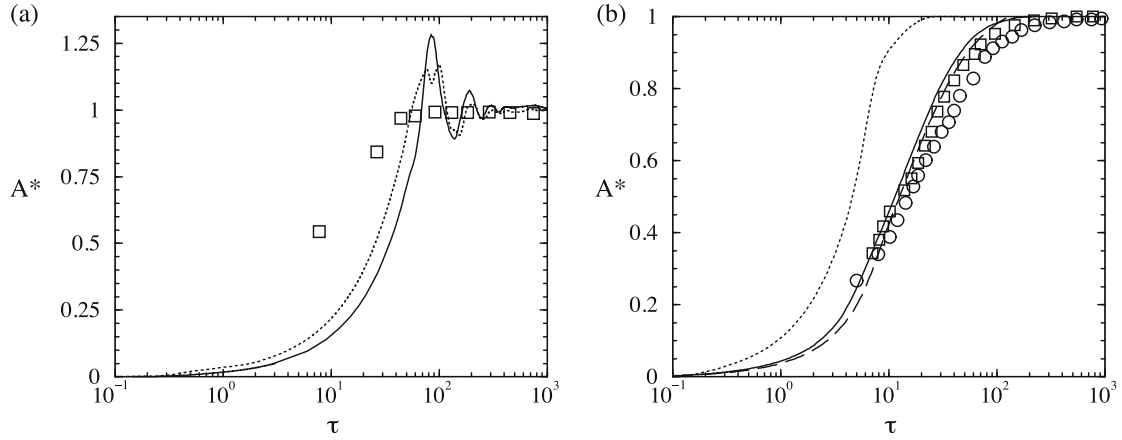


Fig. 15. Evolution of the dimensionless wetted area A^* versus the dimensionless time τ . (a): case LM2. \square experiments, — Simulation using the dynamic model $\theta = \theta_d(t)$, ... Simulation using a constant contact angle $\theta = \theta_s$. (b) Case LM3: \circ experiments, — Simulation using the dynamic model and ... Simulation using a constant contact angle $\theta = \theta_s$. Case LM5: — simulations with dynamic model and \square experiments.

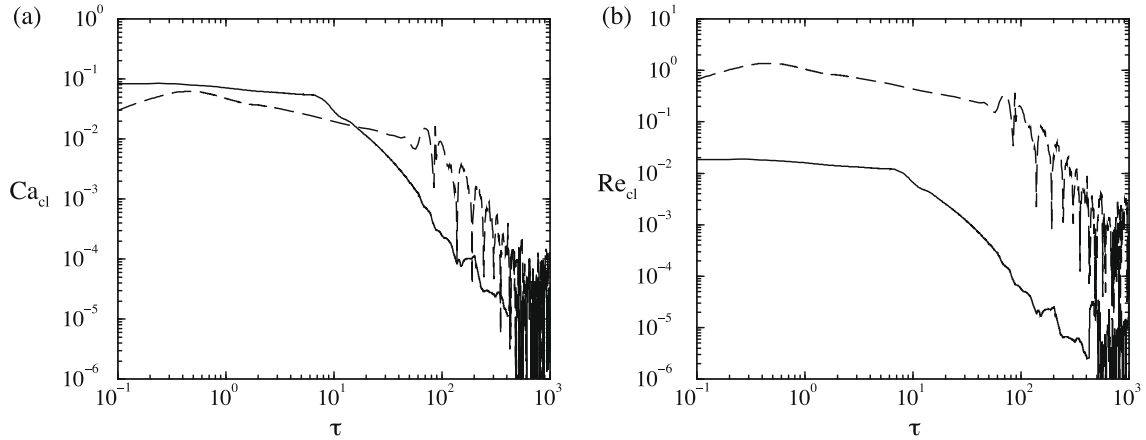


Fig. 16. (a) Evolution of the capillary number $Ca_{cl} = \mu_L |U_{cl}| / \sigma$ and (b) evolution the Reynolds number $Re_{cl} = \rho_L |U_{cl}| r / \mu_L$ versus the dimensionless time τ for the cases: --- LM2, — LM3.

sure that the difference for the case LM2 is not due to the numerical parameters, the grid and time step convergences have been performed and the behaviors are identical to those reported in Section 6.2 for the case LM3. The grid refinement induces a light translation to the right for the time evolution of the contact line position x_{cl} but this effect increases the difference with the experimental values. The time step refinement has no noticeable effect on the time evolution of x_{cl} . We have also performed additional simulations by changing the drop size and its initial position but no significant effect has been observed on the time evolution of x_{cl} . The drop diameter has been divided by 2 (volume divided by 8) and the drop has been initially released at two other positions closer to the wall, $0.97R_0$ and $0.98R_0$.

The inspection of the physical parameters reveals that the case LM2 is characterized by a smaller viscosity of the fluid. This difference can be expressed using the Laplace number $La = 1/Oh^{1/2} = \rho_L \sigma R_0 / \mu_L^2$ which only depends on the physical properties of the problem. This number compares visco-capillarity effects and inertio-capillarity effects. The values of La reported in Table 7 reveals that case LM2 can be considered as inertial while the cases LM3 and LM5 are viscous. This observation leads us to question the validity of the dynamics model used to describe the contact angle. As explained before this model is theoretically valid if $Re_{cl} = \rho_L |U_{cl}| r / \mu_L \ll 1$ and $Ca_{cl} = \mu_L |U_{cl}| / \sigma \ll 1$, [11,33] showing experimentally that the limit of validity can be extended up to $Ca_{cl} \lesssim 0.1$. The corresponding value of Re_{cl} and Ca_{cl} during the spreading are reported in Fig. 16 for cases LM2 and LM3. We clearly observe that the conditions $Re_{cl} \ll 1$ and $Ca_{cl} \ll 1$ are satisfied for LM3 while $Re_{cl} = O(1)$ during the drop spreading for LM2. Consequently, the conditions required for the use of the dynamic model selected for this study are not satisfied for LM2. A correct description of the case LM2 needs the implementation of an inertial model valid for such contact line Reynolds numbers. Our simulation demonstrates the crucial role of the selection of the dynamic model used to simulate a moving contact line.

Fig. 16 illustrates the drop oscillation for the LM2 case before the contact line stabilization. The drop oscillates because of a lower liquid viscosity resulting in a volume oscillation of the drops until all the kinetic energy transmitted to the drop being dissipated. We also observe in this figure that the contact line velocity does not converge to zero but stabilizes around a non zero value. These residual oscillations are characterized by the same Capillary number $Ca_{cl} \approx 2 \times 10^{-5}$ for the two cases LM2 and LM3 while the corresponding Reynolds numbers differ by two orders of magnitude. This is characteristic of the presence of spurious currents generated by the discretization of the surface tension. The residual velocities are discussed in Section 6.5.

6.4. Discussion: dynamic angle versus static angle

In order to stress the importance of the choice of the dynamic model to simulate moving contact lines, the case LM3 is simulated by imposing a constant contact angle equal to the static contact angle $\theta = \theta_s$ during the spreading of the drop, all the others physical and numerical parameters being left unchanged. Note that the use of a no-slip condition ($\lambda = 0$) instead of the slip condition $\lambda = 0.01R_0$ gives very similar results. The shape of the drop during the spreading is compared in Fig. 17 with the results obtained using the dynamic model. We clearly observe a different behavior for the evolution of the shape of the drop. This difference is confirmed by the time evolution of the dimensionless wetted area A^* reported in Fig. 15(b). The difference between the two simulations is spectacular. The spreading of the drop is observed to be faster when imposing the static angle. One order of magnitude is found between the two characteristic times necessary for the complete spreading of the drop. This test shows that it is not possible to reproduce the experiments by imposing the static contact angle with or without a slip condition. This stresses the importance of the contact angle model used for doing simulations of moving contact line. The same comparison is done for the LM2 case in Fig. 15(a). The evolution is also observed to be faster by imposing a constant contact angle but the difference between the static and the dynamic models is found to be less significant in this case.

6.5. Stabilization of the drop: residual spurious velocities

Finally, we characterize the effect of residual spurious currents shown in Fig. 16. For the 3 cases considered we observe a residual oscillation of the contact line but we do not observe contact line destabilization. This is illustrated in Fig. 18 for the



Fig. 17. Shape of the spreading drop (case LM3) at time $\tau = 1.46, 2.92, 4.38, 5.84, 11.7$ and 21.9 . Left: with dynamic model to describe the contact angle ($\theta = \theta_d(t)$). Right: without dynamic model ($\theta = \theta_s$).

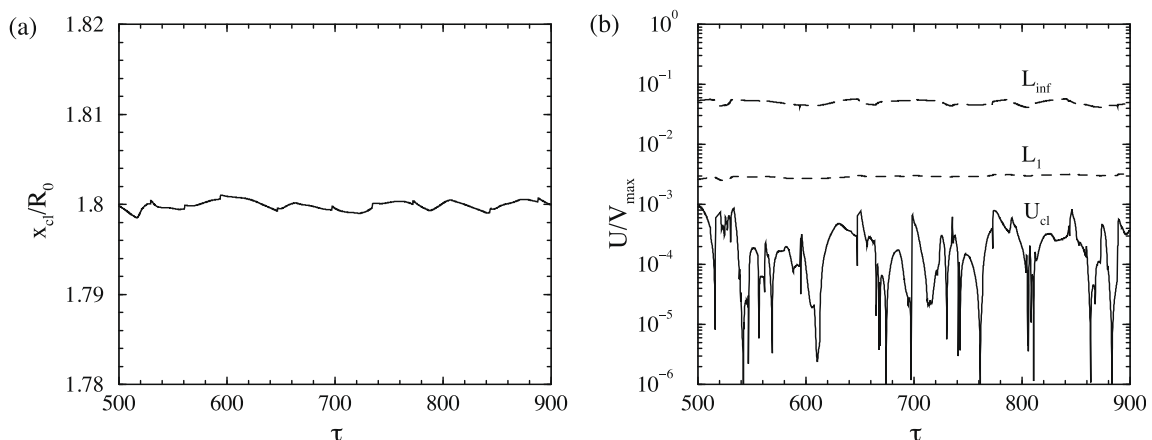


Fig. 18. Stabilization of the contact line at the end of the spreading for the case LM3. (a) Position of the contact line x_{cl} (at $C = 0.5$) normalized by the initial drop radius R_0 versus the dimensionless time τ . (b) Evolution of the residual velocities normalized by the maximal velocity V_{max} . — $|U_{cl}|/V_{max}$, — — ℓ_∞ norm, — — ℓ_1 norm.

Table 8

Characteristic of the residual contact line oscillations.

Case	a_{cl}/x_{cl}	U_{cl} (m/s)	ℓ_∞ (m/s)	ℓ_1 (m/s)
LM2	0.00036	0.00021	0.028	0.0016
LM3	0.00057	0.0000041	0.0046	0.00029
LM5	0.00095	0.0000022	0.0060	0.00021

case LM3. Fig. 18(a) shows the evolution of the position of the interface $x_{cl}(C = 0.5)$ normalized by the initial drop radius R_0 . We clearly observe that a constant position is reached and remains stabilized during more than 10^6 time steps. The contact line stabilizes for $x_{cl}/R_0 \sim 1.8$, value 4% lower than the exact one. We can also notice some very small oscillations with a magnitude a_{cl} less than 0.01% of the mean stabilized position x_{cl} . The magnitude of the velocity $|U_{cl}|$ of the contact line is presented in Fig. 18(b) normalized by the maximum velocity V_{max} measured during the spreading process. We observe that U_{cl} stabilizes around $\approx 2 \times 10^{-4} V_{max}$. We have also reported the measurement of the residual velocity in all the domain using the ℓ_∞ and ℓ_1 norms. We observe that the maximum value of spurious velocities stabilizes around $\approx 4 \times 10^{-2} V_{max} \approx 0.004$ m/s which is close to the estimate (30) $\ell_\infty \approx 0.004\sigma/\mu \sim 0.0038$ m/s proposed in Section 4. The other norm ℓ_1 gives a measure in an average sense for the computational domain. The corresponding stabilized value is $\approx 2 \times 10^{-3} V_{max}$. The velocity of the contact line is thus one order of magnitude less than the ℓ_1 norm and two orders of magnitude less than the ℓ_∞ norm. The values of the amplitude a_{cl} , the contact line velocity U_{cl} , the norms ℓ_∞ and ℓ_1 of the residual velocities are reported in Table 8 for the three cases LM2, LM3 and LM5. The same trend is observed for the three simulations.

6.6. Conclusion

The results presented in this section validate the numerical implementation of the dynamic model chosen to describe moving contact lines. They also stress the importance of the physical model used in numerical simulations to reproduce spreading of drops: (i) the use of a constant static angle (with a no-slip condition or a slip condition) is not appropriate and give significant differences. Our simulations indicate that the use of a constant angle induces a faster spreading, (ii) the dynamic model has to be used with respect to its domain of validity (i.e. viscous or inertial regime).

7. Drop on an inclined wall

We consider here the two-dimensional deformation of a drop placed on a horizontal wall which is slowly inclined. We denote by α the angle between the wall and the initial horizontal position. An hemi-circular drop is initially placed on the wall (see Fig. 6) and its shape evolves to satisfy the equilibrium between gravity, surface tension and the condition imposed by the contact angle at the wall. After the stabilization of the drop, the wall is inclined slowly with a characteristic time larger than the capillarity times defined using viscosity $t_v \sim \mu_L R_0/\sigma$ or using inertia $t_i \sim \sqrt{\rho_L R_0^3/\sigma}$ ensuring that the shape of the drop has the time to adapt to the instantaneous inclination of the wall (i.e. following a quasi-static evolution). The dimensions of the numerical domain are $L \times H = 5 \text{ mm} \times 1 \text{ mm}$ discretized by 400×80 cells. The drop is initially a circular cap of radius $R_0 = H/2$ described by 40 cells. The time step is $\Delta t = 5 \times 10^{-5}$ s. The physical properties used for the following calculations are $\rho_L = 1000 \text{ kg/m}^3$, $\mu_L = 10^{-2} \text{ Pa s}$, $\rho_G = 1 \text{ kg/m}^3$, $\mu_G = 2.10^{-5} \text{ Pa s}$ and $g = 9.81 \text{ m/s}^2$. The surface tension is $\sigma = 0.036 \text{ Nm}^{-1}$, $\sigma = 0.072 \text{ Nm}^{-1}$ or $\sigma = 0.144 \text{ Nm}^{-1}$ so that the Eotvos number $Eo = \rho_L g R_0^2/\sigma$ takes the values $Eo = 0.5, 1$ or 2 , respectively. Different hysteresis angles have been considered: $(\theta_A, \theta_R) = (80^\circ, 100^\circ), (60^\circ, 120^\circ)$ and $(40^\circ, 140^\circ)$.

Fig. 19 shows the shape of the drop when it starts to slide for the different Eotvos numbers and hysteresis considered. The results reveals the strong influence of the parameters (θ_A, θ_R) and Eo on the critical value of α and on the drop shape. Indeed for $Eo = 2$, the drop always starts to move for a critical inclination less than 90° while for $Eo = 0.5$ the drop can stay immobile on the wall up to the vertical position if the hysteresis is large enough. The balance between gravity and capillarity gives the theoretical inclination angle α_{th} with the horizontal line corresponding to the motion of the drop [19,23]:

$$\rho_L A_L g \sin \alpha_{th} = \sigma (\cos \theta_R - \cos \theta_A) \quad (36)$$

where A_L is the area of the two-dimensional drop. The critical angle is thus dependent on the Eotvos number $Eo = \rho_L g R_0^2/\sigma$:

$$\sin \alpha_{th} = \frac{2}{\pi Eo} (\cos \theta_R - \cos \theta_A) \quad (37)$$

The numerical results obtained for the critical angle are compared with the relation (37) in Fig. 20. A very good agreement is found.

Fig. 21 shows the evolution of the shape of the drop during the wall inclination for $Eo = 0.5$ and $(\theta_A, \theta_R) = (60^\circ, 120^\circ)$. The different shapes reported are: the initial hemi-circular shape (time t_0), the initial stabilized shape corresponding to the beginning of the inclination of the wall (time t_1) and the shape when the wall is vertical (time t_2). In this situation the initial circular shape and stabilized shape at the beginning of the wall inclination are nearly the same. During all the wall

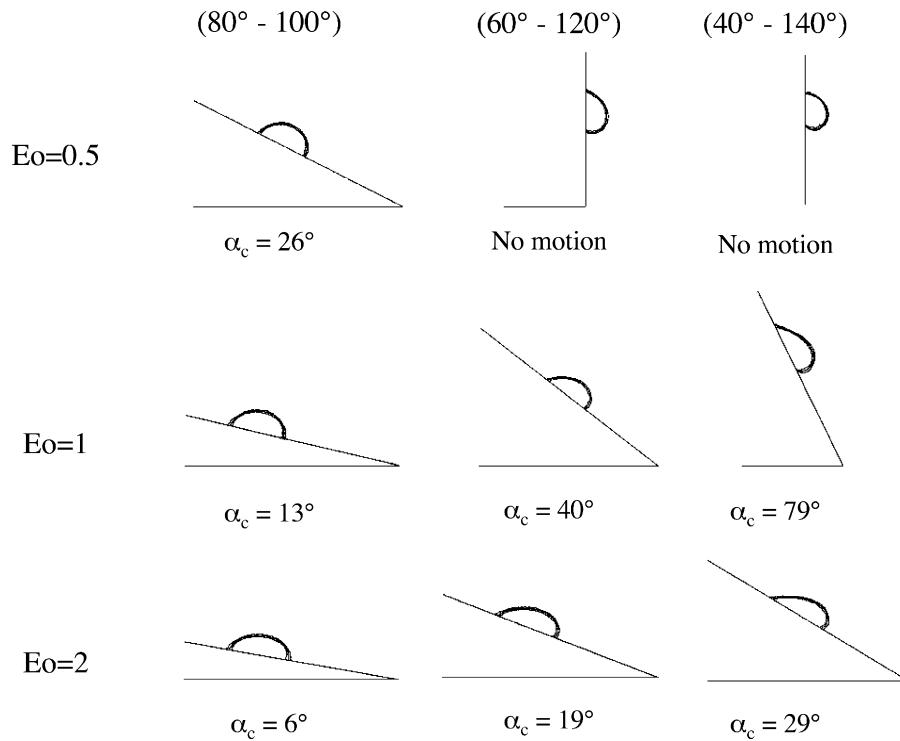


Fig. 19. Shape of the drops at the critical inclination corresponding to beginning of the sliding.

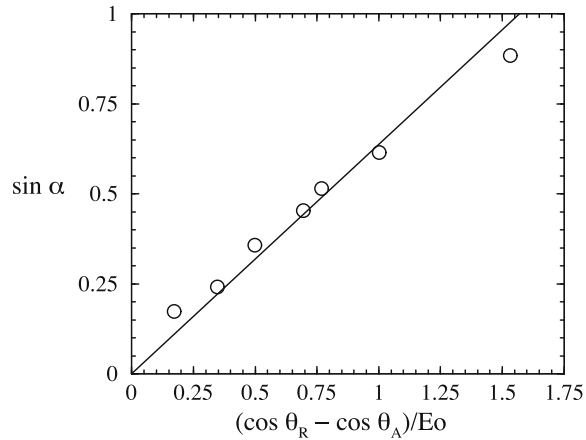


Fig. 20. Critical angle α_{th} versus $(\cos \theta_R - \cos \theta_A)/Eo$. — relation (37). \circ numerical simulations.

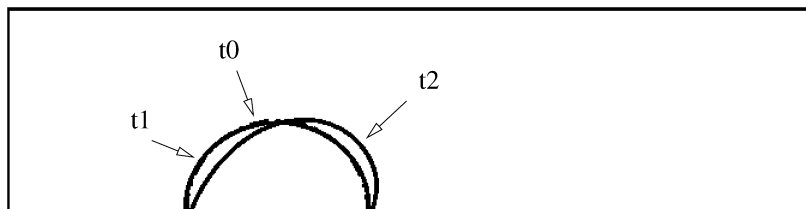


Fig. 21. Drop shape for $Eo = 0.5$ and $(\theta_R, \theta_A) = (60^\circ, 120^\circ)$. Time t_0 (dashed line): initial shape $\alpha = 0^\circ$, time t_1 : beginning of the inclination after the stabilization of the shape of the drop $\alpha = 0^\circ$, time t_2 : deformation for $\alpha = 90^\circ$.

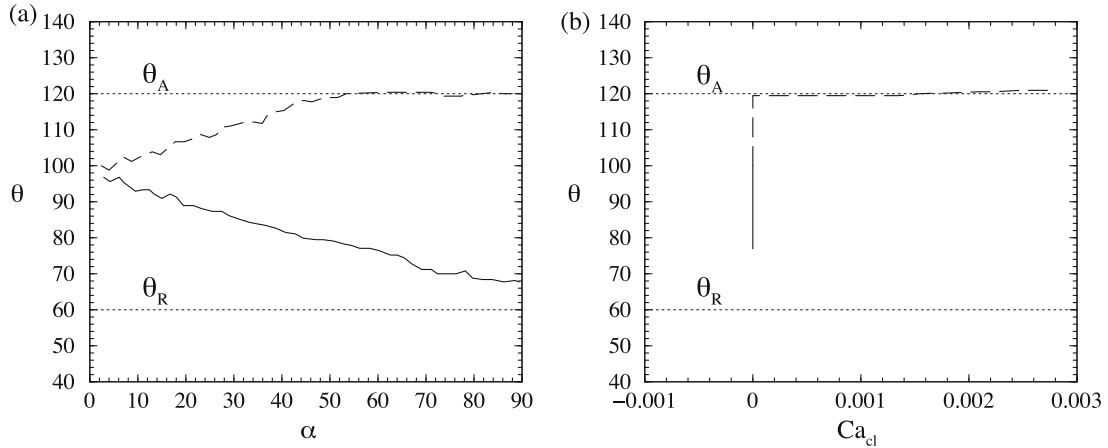


Fig. 22. Advancing and receding contact angles θ_{ad} (---) and θ_{re} (—) for $Eo = 0.5$, $(\theta_R, \theta_A) = (60^\circ, 120^\circ)$ versus: (a) the inclination α of the wall, (b) the Capillary number of the contact line Ca_{cl} .

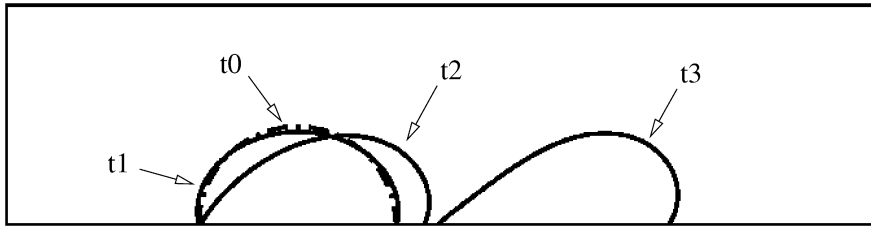


Fig. 23. Evolution the shape of the drop for $Eo = 1$ and $(\theta_R, \theta_A) = (60^\circ, 120^\circ)$. Time t_0 (dashed line): initial shape $\alpha = 0^\circ$, time t_1 : beginning of the inclination after the stabilization of the shape of the drop $\alpha = 0^\circ$, time t_2 : the drop starts to slide on the wall for $\alpha_{num} = 38^\circ$, time t_3 : position and shape for $\alpha \sim 60^\circ$.

inclination, the drop is slightly deformed due to the small value of the Eotvos number and no sliding motion is observed. The corresponding time evolutions of θ_{ad} and θ_{re} , the advancing and receding contact angles, respectively, are reported in Fig. 22(a) versus α . We observe that the drop stabilizes on the horizontal wall for a contact angle close to 100° . Then, when the wall is inclined, the advancing angle θ_{ad} increases progressively and reaches for $\alpha \sim 50^\circ$ the limit angle θ_A and keeps this value until the vertical position of the wall is reached. The receding angle θ_{re} decreases progressively but never reaches the limit angle θ_R . This is the explanation why the drop does not completely slide on the wall although the advancing angle θ_{ad} is equal to θ_A . The corresponding evolutions of θ_{ad} and θ_{re} are reported in Fig. 22(b) versus the local Capillary number $Ca_{cl} = \mu_L U_{cl} / \sigma$ based on the velocity U_{cl} of the contact line. We observe that the receding contact line is always immobile while the advancing contact line slowly starts to move when the advancing angle reaches the limit value θ_A and then stabilizes for the maximum inclination. The consequence is that the drop is slightly stretched but does not slide on the wall. In this case the drop is immobile at the vertical inclination because of the receding angle effect.

We show in Figs. 23 and 24 the same plots for a larger Eotvos number ($Eo = 1$) and the same hysteresis angles. In such situation the motion starts for $\alpha = 38^\circ$. We observe in Fig. 23 a significant deformation when the drop starts to move (time t_2). If we continue to incline the wall, the drop slides on the wall and continues to deform as shown by its position and shapes for $\alpha \sim 60^\circ$ (time t_3). The evolutions of the advancing θ_{ad} and receding θ_{re} angles of the contact line reported in Fig. 24(a) show that the advancing angle θ_{ad} reaches the limit value θ_A before θ_{re} reaches the angle θ_R . We observe that the drop starts to slide on the wall when both θ_{ad} and θ_{re} reach the limit angle θ_A and θ_R , respectively. When the drop is sliding the angle θ_{ad} (resp. θ_{re}) increases (resp. decreases) because of the behavior of the dynamics model given by relation (21). The corresponding evolutions versus the Capillary number Ca_{cl} of the contact angles are reported in Fig. 24(b). It can be seen that the condition of validity of the dynamic model is satisfied since $|Ca_{cl}| \ll 10^{-2}$ during all the evolution. This figure also explains why the variations of the advancing θ_{ad} and receding θ_{re} angles are not symmetric. The two contact lines are not moving at the same speed: the advancing line is moving faster (bigger Ca_{cl}). As a consequence, the length of the wetted surface increases with time as it can be observed in Fig. 23 by comparing the drop shape at time t_2 and t_3 .

8. Drop subjected to a shear flow

We consider in this section the problem of a drop subjected to a shear flow. A Couette flow and a Poiseuille flow are considered (Fig. 25). We first compare and validate our simulations with previous numerical works under creeping flow

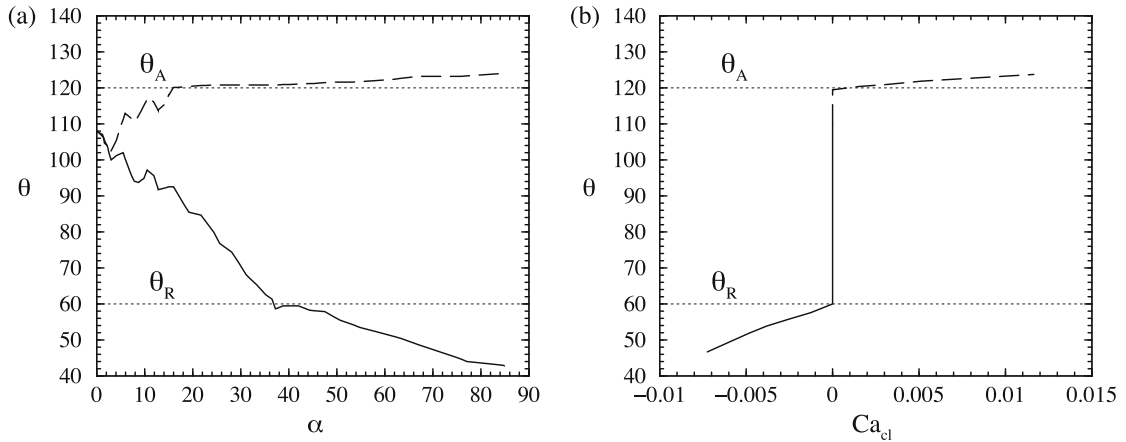


Fig. 24. Advancing and receding contact angles θ_{ad} (---) and θ_{re} (—) for $Eo = 1$, $(\theta_R, \theta_A) = (60^\circ, 120^\circ)$ versus: (a) the inclination α of the wall, (b) the capillary number of the contact line Ca_{cl} .

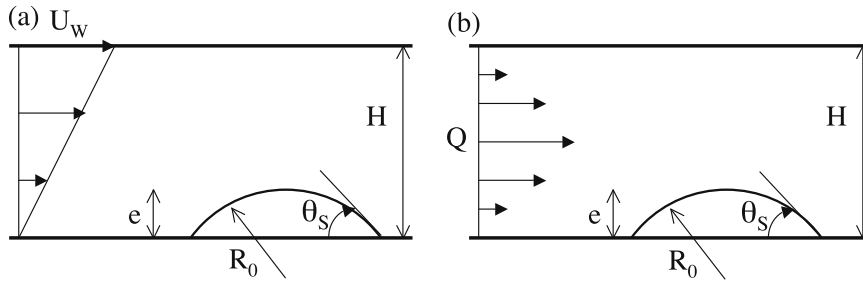


Fig. 25. (a) Circular drop in a Couette flow and (b) circular drop in a Poiseuille flow.

conditions. In the second part we present results concerning the drop deformation and migration in a Poiseuille flow and a criteria is proposed for the drop migration.

8.1. Validation under creeping flow conditions

We first consider the deformation of a drop in a Couette flow (Fig. 25(a)). The objective of this test is to provide additional information concerning the resolution of the contact angle. For this purpose, we compare our simulations with the results obtained by Schleizer and Bonnecaze [52] using a boundary element method. Note that Spelt [55] obtained a very good agreement with this study using a Level Set approach. A circular cap of liquid that satisfies the static contact angle θ_s at the wall (Fig. 25) is initially placed on an immobile wall while the opposite (top) wall moves at a constant velocity U_w . We denote by H the gap between the two walls and e the initial thickness of the drop. This problem is characterized by the ratio e/H , ρ_1/ρ_2 , μ_1/μ_2 , the capillary number $Ca = \mu U_p h / \sigma H$, the Reynolds $Re = \rho U_p h^2 / \mu H$ both based on $U_p h / H$ the velocity of the flow at the top of the drop. For the comparison, the viscosity and the density of the drop are taken to be equal to that of the surrounding fluid ($\rho_1 = \rho_2 = \rho$ and $\mu_1 = \mu_2 = \mu$), the static contact angle is $\theta_s = 60^\circ$ and $e/H = 1/4$. The simulations are performed in a numerical domain of size $6e \times 4e$ described with different grids composed of 60×40 , 120×80 or 180×120 cells, corresponding to 10, 20 and 30 cells in the initial drop height e . The simulations are compared against the Stokes solutions obtained by Schleizer and Bonnecaze [52] for $Ca = 0.05$, $Ca = 0.1$ and $Ca = 0.15$. The corresponding Reynolds numbers are 0.01, 0.02 and 0.03, respectively. A large hysteresis window ($10^\circ - 170^\circ$) is imposed in order to make sure that the drop remains fixed on the wall for the comparison with the corresponding simulations of [52] obtained with fixed contact lines.

Fig. 26 compares the shape calculated by the boundary element method of [52] and the iso-line $C = 0.5$ obtained in our simulations with the 120×80 grid. We observe a very good agreement. The iso-lines $C = 0.05$ and $C = 0.95$ are also represented to quantify the diffusion of the interface. The thickness of the interface is found to be less than 3 cells. A quantitative comparison is estimated by calculating the difference between the numerical y -coordinate $y_k^{C=0.5}$ of the interface ($C = 0.5$) and the corresponding value y^{SB} calculated by Schleizer and Bonnecaze [52] at the same x -coordinates x_k . The standard deviation is normalized by the initial thickness of the drop:

$$E = \frac{1}{e} \sqrt{\frac{1}{N} \sum_{k=1}^N (y_k^{C=0.5} - y^{SB})^2} \quad (38)$$

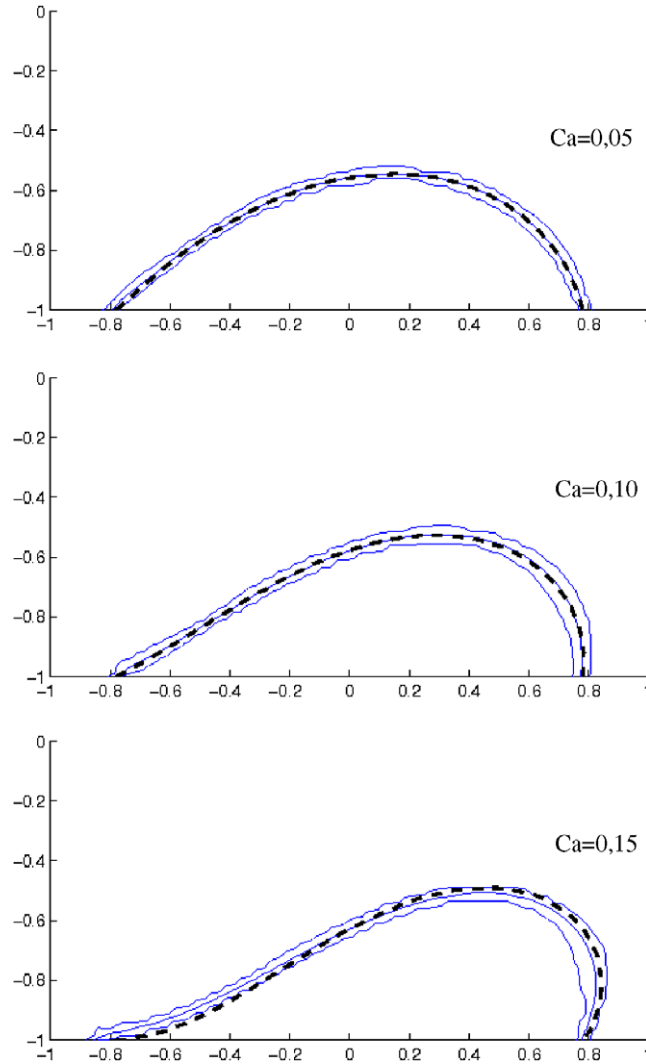


Fig. 26. Comparison with the Stokes solution of [52] for $Ca = 0.05$, $Ca = 0.1$ and $Ca = 0.15$. The bold dashed line are their results. The thin lines are the present results for $C = 0.05$, $C = 0.5$ and $C = 0.95$. The distance on the axis are normalized by $H/2$.

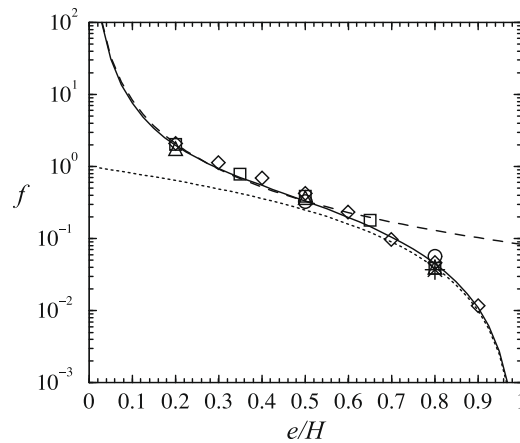
where N is the number of nodes describing the interface. The comparison is performed by digitizing the interface obtained by Schleizer and Bonnecaze [52]. The systematic error made by the software used to digitize the interface has been tested on a hemi-circular shape and has been estimated to be around 0.3%. We have tested different values for N_k and N_l used for the filtering of the capillarity term. We have observed that all the combinations of filtering numbers (N_k, N_l) tested give comparable results. We have also considered the effect of the grid resolution on the results. Three different resolutions have been considered: $e/\Delta y = 10$, $e/\Delta y = 20$ and $e/\Delta y = 30$. The tests were performed for the three capillarity numbers with $N_k = 12$ and $N_l = 6$. The results indicate a satisfactory precision even for a very rough description of the drop $e = 10\Delta y$. The accuracy is found to be similar for $e/\Delta y = 20$ and $e/\Delta y = 30$ showing that a grid corresponding to at least 20 cells per radius is recommended for such simulations. For $Ca = 0.005$ and $Ca = 0.1$, a very good agreement is found ($E \sim 0.5\%$ and $E \sim 1\%$, respectively) and no significant effect of N_k and N_l is observed concerning the shape of the drop. For $Ca = 0.15$ the difference is more important (around 6%). The main difference is the position of the upstream contact line where the value of the contact angle is very small.

8.2. Drop in a Poiseuille channel flow

Here we consider a two-dimensional drop in a channel ($U_w = 0$, Fig. 25). We note H the height of the channel, e the initial height of the drop and Q the gas flow rate. We define the capillary number as $Ca = \mu_l U_G / \sigma$ and the drop Reynolds number as $Re = \rho_G U_G e / \mu_G$ where $U_G = Q/H$ is the mean velocity of the gas in the channel. For the simulations reported below, the

Table 9Critical value of the incident Reynolds number Re_c when the drop starts to move.

Re_c	$(\theta_R, \theta_A) = (80^\circ, 100^\circ)$	$(\theta_R, \theta_A) = (60^\circ, 120^\circ)$	$(\theta_R, \theta_A) = (40^\circ, 140^\circ)$
$e/H = 0.2$	795	1165	1760
$e/H = 0.5$	55	91	106
$e/H = 0.8$	14	24	35

**Fig. 27.** Drop deformation at Re_c for the hysteresis $(80^\circ, 100^\circ)$ (left), $(60^\circ, 120^\circ)$ (centre) and $(40^\circ, 140^\circ)$ (right), for the drop height $h/H = 0.2, 0.4$ and 0.8 .**Fig. 28.** Evolution of $f(e/H) = We_c / (\cos \theta_R - \cos \theta_A)$, $-f(e/H)$ given by relation (40), $-f_1(e/H) = (1 - e/H)^2$, $\dots f_0(e/H) = 1/12(e/H)^2$. Grid 420×80 : $\circ (\theta_R, \theta_A) = (40^\circ, 140^\circ)$, $\triangle (60^\circ, 120^\circ)$, $\square (\theta_R, \theta_A) = (80^\circ, 100^\circ)$; Grid 620×120 : $\star (\theta_R, \theta_A) = (40^\circ, 140^\circ)$, $\diamond (\theta_R, \theta_A) = (80^\circ, 100^\circ)$.

physical parameters are $\rho_L = 1000 \text{ kg/m}^3$, $\mu_L = 10^{-2} \text{ Pa s}$, $\rho_G = 1 \text{ kg/m}^3$, $\mu_G = 2 \cdot 10^{-5} \text{ Pa s}$. The viscosity and density ratios are thus $\mu_L/\mu_G = 500$ and $\rho_L/\rho_G = 1000$, respectively. The computational domain $10H \times H$ is described using 420×80 or 620×120 cells. The time step is $\Delta t = 10^{-6} \text{ s}$. The drop is located at $2.5H$ from the entrance of the domain. The grid is uniform in the region $0 \leq x/H \leq 5$ centered on the drop and the grid spacing is progressively increased using a geometrical progression for $5 \leq x/H \leq 10$. Some simulations have been performed to test the position of the drop relative to the outlet boundary and relative to the entrance of the domain where a parabolic profile is imposed. The mean velocity in the channel U_G is slowly increased from 0 to 20 m/s until that the drop starts to move. The characteristic time of the flow acceleration is chosen to be much larger than the characteristic time of the drop deformation by viscosity $t_v \sim \mu_L h/\sigma$ and inertia $t_i = \sqrt{\rho_L R^3/\sigma}$, respectively. Typically, the time to reach the maximum flow rate is $\sim 100 \text{ ms}$ with a time step $\Delta t = 1 \mu\text{s}$ while $t_v \sim 0.1 \text{ ms}$ and $t_i \sim 1 \text{ ms}$.

Table 9 reports the critical Reynolds number Re_c corresponding to the beginning of the sliding motion of the drop for three hysteresis conditions $(\theta_A, \theta_R) = (100^\circ, 80^\circ)$, $(120^\circ, 60^\circ)$ and $(140^\circ, 40^\circ)$ and three drop heights $e/H = 0.2, 0.5$ and 0.8 . As expected the critical value Re_c decreases when the size of the drop increases, a larger drop being easier to deformed until the advancing and receding contact angles reach their critical values θ_A and θ_R , respectively. For the same reason, Re_c is observed to increase with the magnitude of the hysteresis (difference between θ_A and θ_R) since the capillarity force that maintains the drop on the wall increases with the magnitude of the hysteresis. Fig. 27 reports the shape of the drop at Re_c . This figure reveals that the shape is dependent on both the drop size and the hysteresis condition, the deformation increasing with increasing the hysteresis.

A force balance on the static drop can be used to determine a criteria for the apparition of the sliding motion. Considering the values of the Reynolds numbers reported in Table 9 and the value of the capillary number ($Ca = \mu_G U_G/\sigma < 10^{-3}$), inertia and surface tension are the dominant effects. Consequently, a simple force balance consists in equating the inertia of the incident gas $\sim \rho_G U_G^2 e$ acting on the drop with the capillarity resistance $\sigma(\cos \theta_R - \cos \theta_A)$. Such force balance introduces a critical Weber number $We = \rho_G U_G^2 e/\sigma$ controlled by the hysteresis [56]:

$$We_C \propto (\cos \theta_R - \cos \theta_A)$$

The evolution of the ratio $We_C/(\cos \theta_R - \cos \theta_A)$ reported in Fig. 28 is found to be nearly constant for a given e/H for the two grids used and the three hysteresis conditions. Consequently, We_C evolves linearly with $(\cos \theta_R - \cos \theta_A)$ and Fig. 28 shows that the ratio $We_C/(\cos \theta_R - \cos \theta_A)$ decreases with the value of e/H . The critical Weber number is dependent on e/H in agreement with the dimensional analysis:

$$We_C = f\left(\frac{e}{H}\right)(\cos \theta_R - \cos \theta_A) \quad (39)$$

The numerical values of $f(e/H)$ are reported in Fig. 28. We observe that the behavior at small and large e/H is different. This difference can be intuitively understood since for small values of e/H the perturbation generated in the flow by the drop is small while for larger values of e/H close to unity, the flow is significantly accelerated between the drop and the upper wall due to mass conservation of the gas (Venturi effect). In this situation ($e/H \rightarrow 1$), gas inertia acting on the drop can be estimated by considering the mean velocity $U_c H/(H - e)$ between the top of the drop and the upper wall giving $f_1(e/H) = (1 - e/H)^2$. For small drops ($e/H \rightarrow 0$), the effect of the fluid inertia can be estimated by the integration from $y = 0$ to $y = e$ of the parabolic incident velocity given $f_0(e/H) = 1/12(e/H)^2$.

Fig. 28 clearly shows that these two functions are effectively the two asymptotic limits for the evolution of $f(e/H)$. A simple fitting function $f(e/H)$ can be deduced from these two evolutions:

$$f\left(\frac{e}{H}\right) = \left[1 + f_0\left(\frac{e}{H}\right)\right]f_1\left(\frac{e}{H}\right) \quad (40)$$

as shown by Fig. 28.

9. Conclusion

In this paper, a numerical “macroscopic-scale” method to describe static (including hysteresis) and moving contact lines for partially wetting liquids has been presented and tested in several well controlled situations. The numerical method is based on the implementation of the apparent angle observed at intermediate length scales. A “sub-grid” description of the contact line consists in imposing the apparent angle for the hysteresis as well as for the dynamic description of a moving line. For this purpose a dynamic model valid for viscous contact line regimes has been implemented. Note that any other dynamic model for moving contact line [12,20,26] can be readily introduced in our code. The code is now able to be used for a comparison of these different dynamics model with experiments of liquid spreading on solid surfaces. The choice of the grid size at the wall is imposed by the physical length scale introduced to cut off the singularity of the contact line corresponding to the intermediate scale $\Delta x \sim r \sim 10 \mu\text{m}$. The developed procedure is similar to a ghost description at the wall and it can be implemented in any numerical methods with no interface reconstruction algorithm (VoF, Level Set). The numerical model has been tested by comparison with analytical solutions, numerical simulations or experiments for different situations: the equilibrium shape of a drop released on a hydrophobic or hydrophilic wall, the axisymmetric spreading of a drop for a partially wetting liquid, the migration of a drop placed on a wall that is slowly inclined and finally a drop submitted to a Couette or Poiseuille flow. The agreement has been found very satisfactory and shows that our code is able to simulate problems controlled by the contact line with a relative moderate grid resolution.

In the discussion of the results, it has been pointed out that simulations of moving contact line cannot be performed using a static constant angle with a no-slip condition at the wall. The choice of the dynamic model used to describe a moving contact line is also important and simulations have to be performed respecting the range of validity imposed by the selected physical modeling.

Acknowledgments

We are grateful to Peter Spelt for several interesting discussions on moving contact line modeling and for a careful reading of the manuscript. We would like to acknowledge RENAULT (Technocentre, Guyancourt, France) and ADEME for the financial support of this work.

References

- [1] S. Afkhami, M. Bussmann, Height functions for applying contact angles to 2D VOF simulations, *Int. J. Num. Meth. Fluids* 57 (2008) 453–472.
- [2] S. Afkhami, S. Zaleski, M. Bussmann, A mesh-dependent model for applying dynamic contact angles to VOF simulations, *J. Comput. Phys.* 228 (15) (2009) 5370–5389.
- [3] A. Benkennedj, J. Magnaudet, Une méthode de simulation d'écoulements diphasiques sans reconstruction d'interface, *C.R. Acad. Sci. (II b)* 328 (2000) 25–32.
- [4] T.D. Blake, The physics of moving wetting lines, *J. Colloid Interface Sci.* 299 (2006) 1–13.
- [5] T.D. Blake, J.M. Haynes, Kinetics of liquid/liquid displacement, *J. Colloid Interface Sci.* 30 (1969) 421.
- [6] T. Bonometti, Développement d'une méthode de simulation d'écoulements à bulles et à gouttes, Ph.D. Thesis, INP Toulouse, France, 2006.
- [7] T. Bonometti, J. Magnaudet, Transition from spherical cap to toroidal bubbles, *Phys. Fluids* 18 (2006) 052102.
- [8] T. Bonometti, J. Magnaudet, An interface capturing method for incompressible two-phase flows. Validation and application to bubble dynamics, *Int. J. Multiphase Flow* 33 (2) (2007) 109–133.

- [9] J. Brackbill, D.B. Kothe, C. Zemach, A continuum method for modeling surface tension, *J. Comput. Phys.* 100 (1992) 335–354.
- [10] I. Calmet, J. Magnaudet, Large-eddy simulation of high-Schmidt number mass transfer in a turbulent channel flow, *Phys. Fluid* 9 (2) (1997) 438–455.
- [11] Q. Chen, E. Ramé, S. Garoff, The breakdown of asymptotic hydrodynamic models of liquid spreading at increasing capillary number, *Phys. Fluid* 7 (11) (1995) 2631–2639.
- [12] R.G. Cox, On the dynamics of liquid spreading on solid surfaces, *J. Fluid. Mech.* 209 (1998) 191–226.
- [13] R.G. Cox, The dynamics of the spreading of liquids on a solid surface. Part 1: viscous flow, *J. Fluid. Mech.* 168 (1986) 169.
- [14] P. Dimitrakopoulos, J.J.L. Higdon, On the displacement of three-dimensional fluid droplets adhering to a plane wall in viscous pressure driven flows, *J. Fluid Mech.* 435 (2001) 327–350.
- [15] H. Ding, P.D.M. Spelt, Inertial effects in droplets spreading: a comparison between diffuse-interface and Level-Set simulations, *J. Fluid Mech.* 576 (2007) 287–296.
- [16] H. Ding, P.D.M. Spelt, Onset of motion of a three-dimensional droplet on a wall in shear flow at moderate Reynolds number, *J. Fluid Mech.* 599 (2008) 341–362.
- [17] V.C.G. Dussan, On the spreading of liquids on solid surfaces: static and dynamic contact lines, *Ann. Rev. Fluid. Mech.* 11 (1979) 371–400.
- [18] V.C.G. Dussan, E. Ramé, S. Garoff, On identifying the appropriate boundary conditions at a moving contact line: an experimental investigation, *J. Fluid Mech.* 230 (1991) 97–116.
- [19] V.C.G. Dussan, R.T.-P. Chow, On the ability of drops or bubbles to stick to non-horizontal surfaces of solids, *J. Fluid Mech.* 137 (1983) 1–29.
- [20] J. Eggers, Towards a description of contact line motion at higher capillary numbers, *Phys. Fluid* 16 (9) (2004) 3491–3494.
- [21] D.E. Finlow, P.R. Kota, A. Bose, Investigation of wetting hydrodynamics using numerical simulations, *Phys. Fluid* 8 (2) (1996) 302.
- [22] M.M. Francois, S.J. Cummins, E.D. Dendy, D.B. Kothe, J.M. Sicilian, M.W. Williams, A balanced-force algorithm for continuous and sharp interfacial surface tension models within a volume tracking framework, *J. Comput. Phys.* 213 (2006) 141–173.
- [23] C.G.L. Furmidge, Studies at phase interfaces. The sliding of liquid drops on solid surfaces and theory for spray retention, *J. Colloid Sci.* 17 (1962) 309–324.
- [24] P.-G. de Gennes, Wetting: statics and dynamics, *Rev. Mod. Phys.* 57 (1985) 827.
- [25] P.-G. de Gennes, Deposition of Langmuir–Blodgett layers, *Colloid Polym. Sci.* 264 (1986) 463–465.
- [26] P.-G. de Gennes, X. Hua, P. Levinson, Dynamics of wetting: local contact angles, *J. Fluid Mech.* 212 (1990) 55–63.
- [27] K.B. Glasner, A boundary integral formulation of quasi-steady fluid wetting, *J. Comput. Phys.* 207 (2005) 529–541.
- [28] C. Huh, L.E. Scriven, Hydrodynamic model of steady movement of a solid/liquid/fluid contact line, *J. Colloid Interface Sci.* 35 (1971) 85.
- [29] D. Jacqmin, Contact-line dynamics of a diffusive fluid interface, *J. Fluid Mech.* 402 (2000) 57–88.
- [30] D. Jamet, D. Torres, J.U. Brackbill, On the theory and computation of surface tension: the elimination of parasitic currents through energy conservation in the second-gradient method, *J. Comput. Phys.* 182 (2002) 262–276.
- [31] M. Khennar, Computation of the material indicator function near the contact line (in Tryggvason's method), *J. Comput. Phys.* 200 (2004) 1–7.
- [32] B. Lafaurie, C. Nardone, R. Scardovelli, S. Zaleski, G. Zanetti, Modelling merging and fragmentation in multiphase flows with SURFER, *J. Comput. Phys.* 113 (1994) 134–147.
- [33] B. Lavi, A. Marmur, The exponential power law: partial wetting kinetics and dynamic contact angles, *Colloid Surf. A* 250 (2004) 409–414.
- [34] D. Legendre, J. Magnaudet, The lift force on a spherical bubble in a viscous linear shear flow, *J. Fluid Mech.* 368 (1998) 81–126.
- [35] D. Legendre, J. Magnaudet, G. Mougin, Hydrodynamic interactions between two spherical bubbles rising side by side in a viscous liquid, *J. Fluid Mech.* 497 (2003) 133–166.
- [36] D. Legendre, C. Colin, Enhancement of wall-friction by fixed cap-bubbles, *Phys. Fluids* 20 (2008) 051704.
- [37] D. Legendre, E. Lauga, J. Magnaudet, Influence of slip on the dynamics of two-dimensional wakes, *J. Fluid. Mech.* 633 (2009) 437–447.
- [38] H. Liu, S. Krishnan, S. Marella, H.S. Udaykumar, Sharp interface Cartesian grid method II: a technique for simulating droplets interactions with surfaces of arbitrary shape, *J. Comput. Phys.* 210 (2005) 32–54.
- [39] A. Marmur, Equilibrium and spreading of liquids on solid surfaces, *Adv. Colloid Interf. Sci.* 19 (1983) 75–102.
- [40] B. Mathieu, Etudes physiques, expérimentale et numérique des mécanismes de base intervenant dans les écoulements diphasiques en micro-fluidique, Thèse de Doctorat, Université de Provence-Marseille, France, 2003.
- [41] J. Magnaudet, M. Rivero, J. Fabre, Accelerated flows past a rigid sphere or a spherical bubble. Part 1. Steady straining flow, *J. Fluid Mech.* 284 (1995) 97–135.
- [42] J.A. Marsh, S. Garoff, E.B. Dussan, Dynamic contact angles and hydrodynamics near a moving contact line, *Phys. Rev. Lett.* 70 (18) (1993) 2778–2782.
- [43] A. Merle, D. Legendre, J. Magnaudet, Forces on a high-Re spherical bubble in a turbulent flow, *J. Fluid Mech.* 532 (2005) 53–62.
- [44] C.L. Navier, Sur les lois du mouvement des fluides, *Mem. Acad. R. Sci. France* 6 (1823) 389–440.
- [45] C.G. Ngan, E.B. Dussan, On the dynamics of liquid spreading on solid surfaces, *J. Fluid Mech.* 209 (1989) 191–226.
- [46] S. Popinet, S. Zaleski, A front-tracking algorithm for accurate representation of surface tension, *Int. J. Numer. Meth. Fluid* 30 (1999) 775–793.
- [47] M. Renardy, Y. Renardy, J. Li, Numerical simulation of moving contact line problems using a volume-of-fluid method, *J. Comput. Phys.* 171 (2001) 243–263.
- [48] Y. Renardy, M. Renardy, PROST: a parabolic reconstruction of surface tension for the volume-of-fluid method, *J. Comput. Phys.* 183 (2002) 400–421.
- [49] J. Sethian, *Level Set Methods and Fast Marching Methods*, Cambridge University Press, Cambridge, 1999.
- [50] M. Sussman, E. Fatemi, P. Smereka, S. Osher, A Level Set approach for computing solutions in incompressible two-phase flows, *Comput. Fluids* 27 (1998) 663–680.
- [51] R. Scardovelli, S. Zaleski, Direct numerical simulation of free surface and interfacial flow, *Ann. Rev. Fluid Mech.* 31 (1999) 567.
- [52] A.D. Schleizer, R.T. Bonnecaze, Displacement of a two-dimensional immiscible droplet adhering to a wall in shear and pressure-driven flow, *J. Fluid Mech.* 383 (1999) 29–54.
- [53] C. Shen, D.W. Ruth, Experimental and numerical investigations of the interface profile close to a moving contact line, *Phys. Fluid* 331 (7) (1998) 509–514.
- [54] Y.D. Shikhmurzaev, Moving contact lines in liquid/liquid/solid systems, *J. Fluid Mech.* 334 (1997) 211–249.
- [55] P.D.M. Spelt, A Level-Set approach for simulations of flows with multiple moving contact lines with hysteresis, *J. Comput. Phys.* 207 (2005) 389–404.
- [56] P.D.M. Spelt, Shear flow past two-dimensional droplets pinned or moving on an adhering channel wall at moderate Reynolds numbers: a numerical study, *J. Fluid Mech.* 561 (2006) 439–463.
- [57] O.V. Voinov, Hydrodynamics of wetting, *Fluid Dyn.* 11 (5) (1976) 714.
- [58] S.T. Zalesak, Fully multidimensional flux-corrected transport algorithms for fluids, *J. Comput. Phys.* 31 (1979) 335–362.
- [59] A. Zosel, Studies of the wetting kinetics of liquid drops on solid surfaces, *Colloid Polym. Sci.* 271 (1993) 680–687.